RESEARCH ARTICLE | JANUARY 08 2025

The generation of whistler, lower hybrid, and magnetosonic waves by satellites passing through ionospheric magnetic field aligned irregularities

Bengt Eliasson ; Paul A. Bernhardt

Phys. Plasmas 32, 012103 (2025)
https://doi.org/10.1063/5.0225399

Physics of Plasmas ARTICLE pubs.aip.org/aip/pop

The generation of whistler, lower hybrid, and magnetosonic waves by satellites passing through ionospheric magnetic field aligned irregularities

Cite as: Phys. Plasmas **32**, 012103 (2025); doi: 10.1063/5.0225399
Submitted: 24 June 2024 · Accepted: 9 December 2024 ·
Published Online: 8 January 2025

Bengt Eliasson[1,a)] and Paul A. Bernhardt[2]

AFFILIATIONS

[1]Department of Physics, SUPA, University of Strathclyde, Glasgow G4 0NG, United Kingdom
[2]Geophysical Institute, University of Alaska, Fairbanks, Alaska 99775, USA

[a)]Author to whom correspondence should be addressed: bengt.eliasson@strath.ac.uk

ABSTRACT

A numerical study is carried out for the generation of lower hybrid, whistler, and compressional Alfvén (magnetosonic) waves by satellites crossing magnetic field aligned irregularities or striations. Satellites and space debris propagating at an altitude of about 300 km with a velocity of 7.7 km/s perpendicular to the magnetic field generate a wake of lower hybrid waves with a wavelength of ∼1 m and frequencies near the lower hybrid frequency ∼7.87 kHz. In the presence of small-scale striations having widths below 0.5 m, the satellite-generated lower hybrid waves efficiently mode convert to whistler waves with frequencies slightly above the lower hybrid frequency, which propagate within a cone ∼19.5° to the background magnetic field. For larger striations having widths of 1 m and above, the interaction with satellites leads to modulated pulses of whistler waves as well as to magnetosonic waves propagating at large angles to the magnetic field, with frequencies below the lower hybrid frequency. The results are consistent with recent observations during conjunctures between satellites, where the observed frequencies ranged from the ion cyclotron frequency to the lower hybrid frequency [Bernhardt *et al.*, Phys. Plasmas **30**, 092106 (2023)].

I. INTRODUCTION

Recent observations have shown wave activity during conjunction between satellites, with frequencies ranging from the ion cyclotron frequency to the lower hybrid (LH) frequency (Bernhardt *et al.*, 2023). A possible mechanism is that the satellites become electrically charged and interact with the plasma to generate the observed waves. Objects in space become electrically charged by collecting electrons from the surrounding plasma or by photoemission of electrons due to UV radiation from the sun (Garrett, 1981; Whipple, 1981; and Anderson, 2012). The charging of an object in plasma depends on the balance between electron and ion currents reaching the object, such as for Langmuir probes (Langmuir and Mott-Smith, 1926; Chen, 1965; Hutchinson, 2002; and Merlino, 2007), dusty (or complex) plasma (Rao *et al.*, 1990; Shukla and Eliasson, 2009; Bernhardt *et al.*, 1995a; and Beckers *et al.*, 2023), and man-made spacecraft and space debris (Anderson, 2012; Bernhardt *et al.*, 2023). At the floating potential relative to the surrounding plasma, the electron and ion currents cancel each other, $I_i + I_e = 0$. The charged objects may work as a current source for Cherenkov radiation of low frequency (LF) plasma waves with a possibility of using the waves for detecting and diagnosing the objects. Many previous theoretical works have suggested that hypersonic space objects can launch ion acoustic solitons [e.g., Truitt and Hartzell (2020a); (2020b)] but Bernhardt *et al.* (2023) points out that these ion acoustic waves have never been observed. In addition, these waves are highly attenuated by ion Landau damping as discussed in Appendix A of this paper. This work focusses on lower hybrid, magnetosonic (MS), and whistler waves that have been detected with *in situ* electric field measurements and are unaffected by ion Landau damping.

Magnetic field aligned striations are almost always formed during ionospheric heating experiments [e.g., Kelley *et al.* (1995); Bernhardt *et al.* (1995b); and Najmi *et al.* (2014), (2015)]. Due to the different electron mobility perpendicular and parallel to the magnetic field, the striations can have transverse length scales of a few meters or less, while the parallel length scale is tens of kilometers. The striations work as scattering centers to mode convert lower hybrid waves to whistler waves (Eliasson and Papadopoulos, 2008; Camporeale *et al.*, 2012) and vice versa (Bell and Ngo, 1990; Rosenberg and Gekelman, 1998; and Shao *et al.*, 2012).

The aim of the present paper is to numerically and theoretically investigate the interaction between satellites propagating perpendicular to the magnetic field and interacting with magnetic field aligned irregularities to generate lower hybrid, whistler, and magnetosonic waves and how these can be observed and analyzed by other spacecraft, to determine the distance and direction to the satellite. Since magnetic field aligned striations, of natural origin or generated during ionospheric heating experiments, extend tens of km above the heated region, they may constitute a means of detecting and diagnosing satellites propagating through bunches of striations and emitting very low frequency (VLF) waves.

The paper is organized in the following fashion. Section II discusses the cold fluid plasma model for the VLF waves with frequencies higher than the ion cyclotron frequency and derives a wave equation suitable for numerical simulations. The wave dispersion properties of the model are discussed in Sec. III, where it is shown that the model supports, lower hybrid, magnetosonic waves, and whistler waves up to the electron cyclotron frequency. Wave generation and mode conversion of lower hybrid waves on striations are discussed. A simple satellite charging model based on spherical symmetry is derived in Sec. IV, which is used in the numerical simulations. Section V describes the 2D simulation model and presents simulation results for different sizes of satellites and striations to identify the efficiency of the different generation mechanisms of lower hybrid, whistler, and magnetosonic waves. Frequency spectra of simulated waves are compared to recent spacecraft observations. A method to detect and locate space debris via dispersion properties of waves and Poynting flux is proposed. Finally, Sec. VI contains a summary of the results and discusses future works to equip spacecraft with instruments to enable detection and localization of space debris.

II. IONOSPHERIC PLASMA MODEL

The linearized cold plasma fluid model supports VLF waves with frequencies higher than the ion cyclotron frequency but lower than the light mode and Langmuir oscillations. The momentum equations for the ion and electron fluid velocities $\mathbf{v}_i$ and $\mathbf{v}_e$ read

$$m_i \frac{\partial \mathbf{v}_i}{\partial t} = e\mathbf{E}, \tag{1}$$

$$m_e \frac{\partial \mathbf{v}_e}{\partial t} = -e(\mathbf{E} + \mathbf{v}_e \times \mathbf{B}_0), \tag{2}$$

where $\mathbf{B}_0$ is the background magnetic field, e is the unit charge, $\mathbf{B}_0$ is the background magnetic field, and m_i and m_e are the ion and electron mass, respectively. The $\mathbf{v}_i \times \mathbf{B}_0$ term has been neglected in Eq. (1) due to the assumption that the typical wave frequency ω is much larger than the ion cyclotron frequency $\omega_{ci} = eB_0/m_i$. The wave electric and magnetic fields $\mathbf{E}$ and $\mathbf{B}$ are governed by Faraday's and Ampère's laws,

$$\frac{\partial \mathbf{B}}{\partial t} = -\nabla \times \mathbf{E}, \tag{3}$$

$$\nabla \times \mathbf{B} = \mu_0 e\tilde{n}(\boldsymbol{r}_\perp)(\mathbf{v}_i - \mathbf{v}_e) + \mu_0 \mathbf{v}_{\rm sat}\, \rho_{\rm sat}(\boldsymbol{\xi}), \tag{4}$$

where the plasma density including magnetic field aligned striations is $\tilde{n}(\boldsymbol{r}_\perp) = n_0 + n_{\rm str}(\mathbf{r}_\perp)$ with n_0 being the background density and $n_{\rm str}(\mathbf{r}_\perp) = -n_{0,\,\rm str}\exp\left(-r_\perp^2/D_{\rm str}^2\right)$ representing a magnetic field aligned density reduction (striation) and $\mathbf{r}_\perp$ is the space coordinate perpendicular to $\mathbf{B}_0$, and where $n_{0,\,\rm str}$ is the magnitude of the striation density and $D_{\rm str}$ is the striation width. The magnetic field aligned striations are formed and evolve very slowly in time on the order of seconds or more [e.g., Grach *et al.* (2016)] and are, therefore, here regarded as stationary. Furthermore, $\mu_0 = 1/\epsilon_0 c^2$ is the vacuum magnetic permeability, ϵ_0 is the vacuum electric permittivity, and c is the speed of light. The satellite constitutes a local current density pulse that creates time-dependent magnetic and electric fields which can interact with the plasma particles to generate waves. For computational efficiency, the charge distribution of the satellite is represented as a Gaussian density pulse of the form $\rho_{\rm sat}(\boldsymbol{\xi}) = \rho_{0\rm sat}\exp(-\xi^2/D_{\rm sat}^2)$ using the shifted space variable $\boldsymbol{\xi} = \mathbf{r} - \mathbf{v}_{\rm sat}t$ with $\mathbf{v}_{\rm sat}$ being the satellite velocity; hence, the current density of the satellite enters as $\mathbf{v}_{\rm sat}\,\rho_{\rm sat}(\boldsymbol{\xi})$ in Eq. (4). The displacement current has been neglected in Eq. (4) by assuming wave speeds much smaller than the speed of light and by assuming quasi-neutrality $n_{\rm i} = n_{\rm e}$, which is justified for $\omega_{\rm pe}^2 \gg \omega_{\rm ce}^2$ where $\omega_{\rm pe}$ and ω_{ce} are the electron plasma and cyclotron frequencies (cf. Table I). As shown in Sec. III below, the model (1)–(4) supports lower hybrid waves, whistler waves, and compressional Alfvén/magnetosonic waves with frequencies much higher than the ion cyclotron frequency.

By defining the electron number current density (Eliasson and Papadopoulos, 2008), $\tilde{n}(\boldsymbol{r}_\perp)\mathbf{v}_e \equiv \mathbf{j}_e$ is a single wave equation suitable for numerical simulation is derived (see Appendix B)

$$\left(1 - \lambda_e^2\nabla^2\right)\frac{\partial \mathbf{j}_e}{\partial t} + \underbrace{\frac{\rm e}{m_e}\lambda_{\rm e}^2\nabla \times \left(\nabla \times \left(\frac{\mathbf{j}_{\rm e} \times \mathbf{B}_0}{\tilde{n}(\boldsymbol{r}_\perp)/n_0}\right)\right)}_{\text{Whistler}} - \frac{e}{m_i}\lambda_{\rm e}^2\nabla(\nabla \cdot (\mathbf{j}_{\rm e} \times \mathbf{B}_0)) + \frac{e}{m_i}\mathbf{j}_{\rm e} \times \mathbf{B}_0 \underbrace{- \frac{1}{e}\left(\mathbf{v}_{\rm sat}\frac{\partial}{\partial t} + \lambda_e^2\nabla\frac{\partial^2}{\partial t^2}\right)\rho_{\rm sat}(\boldsymbol{\xi})}_{\text{Satellite}} = 0, \tag{5}$$

Lower hybrid+magnetosonic

where the terms associated with different wave modes are indicated, as well as the Satellite terms which work as sources.

Ionospheric parameters used in the simulations are consistent with High-frequency Active Auroral Research Program (HAARP) conditions near 300 km altitude and are listed in Table I, including the magnetic field strength $B_0 = 4.8 \times 10^{-5}$ T (at HAARP, $\mathbf{B}_0$ is directed downwards 14° to the vertical), and the background plasma number density $n_0 = 5.0 \times 10^{11}\ \mathrm{m}^{-3}$. The ions are oxygen O^+ with a mass $m_i = 26.57 \times 10^{-27}$ kg. This gives a number of derived plasma parameters listed in Table I. The approximate expression for the lower hybrid frequency $\omega_{\rm LH} = \sqrt{\omega_{\rm ce}\omega_{\rm ci}}$ is valid for high electron density and low magnetic field such that $\omega_{\rm pe}^2 \gg \omega_{\rm ce}^2$ so that quasineutrality

TABLE I. Parameters used in the ionospheric plasma model.

Parameter	Symbol/formula and value
Plasma number density	$n_0 = 5 \times 10^{11}\ \mathrm{m}^{-3}$
Geomagnetic field	$B_0 = 4.8 \times 10^{-5}\ \mathrm{T}$
Ion mass, oxygen O^+	$m_\mathrm{i} = 26.57 \times 10^{-27}\ \mathrm{kg}$
Electron plasma frequency	$\omega_\mathrm{pe} = \sqrt{\frac{n_0 e^2}{\epsilon_0 m_\mathrm{e}}} = 39.9 \times 10^6\ \mathrm{s}^{-1}$ $(f_\mathrm{pe} = 6.36\ \mathrm{MHz})$
Ion plasma frequency	$\omega_\mathrm{pi} = \sqrt{\frac{n_0 e^2}{\epsilon_0 m_\mathrm{i}}} = 234 \times 10^3\ \mathrm{s}^{-1}$ $(f_\mathrm{pi} = 37.2\ \mathrm{kHz})$
Electron cyclotron frequency	$\omega_\mathrm{ce} = eB_0/m_\mathrm{e} = 8.44 \times 10^6\ \mathrm{s}^{-1}$ $(f_\mathrm{ce} = 1.34\ \mathrm{MHz})$
Ion cyclotron frequency	$\omega_\mathrm{ci} = eB_0/m_\mathrm{i} = 289\ \mathrm{s}^{-1}$ $(f_\mathrm{ci} = 46.1\ \mathrm{Hz})$
Lower hybrid frequency (for $\omega_\mathrm{pe}^2 \gg \omega_\mathrm{ce}^2$)	$\omega_\mathrm{LH} = \sqrt{\omega_\mathrm{ce}\omega_\mathrm{ci}} = 49.4 \times 10^3\ \mathrm{s}^{-1}$ $(f_\mathrm{LH} = 7.87\ \mathrm{kHz})$
Electron inertial length	$\lambda_\mathrm{e} = c/\omega_\mathrm{pe} = 7.52\ \mathrm{m}$
Ion inertial length	$\lambda_\mathrm{i} = c/\omega_\mathrm{pi} = 1.28\ \mathrm{km}$
Alfvén speed	$v_\mathrm{A} = c\frac{\omega_{ci}}{\omega_{pi}} = \omega_{ci}\lambda_i = \omega_{LH}\lambda_e = 372\ \mathrm{km/s}$
Satellite speed	$v_\mathrm{sat} = 7.7\ \mathrm{km/s}$
Striation depth	$n_{0,\mathrm{str}} = 0.05\, n_0 = 0.25 \times 10^{11}\ \mathrm{m}^{-3}$
Electron temperature, satellite charging model	$T_\mathrm{e} = 1500\ \mathrm{K}$
Debye length, satellite charging model	$\lambda_\mathrm{De} = \sqrt{\frac{\epsilon_0 k_B T_e}{n_0 e^2}} = 0.0038\ \mathrm{m}$

$n_\mathrm{i} = n_\mathrm{e}$ holds by electrons performing polarization drift perpendicular to the magnetic field to neutralize the ions in the lower hybrid wave. For larger magnetic field or lower density such that ω_ce^2 is comparable to ω_pe^2, the electrons cannot drift to neutralize the ion fluctuations completely, and deviation from quasineutrality needs to be taken into account via Gauss' law $\nabla \cdot \mathbf{E} = e(n_i - n_e)/\epsilon_0$ for the electric field and the ion and electron continuity equations $\partial n_{\mathrm{i,e}}/\partial t + n_0 \nabla \cdot \mathbf{v}_{\mathrm{i,e}} = 0$, leading to [e.g., Swanson (2003)] $\omega_\mathrm{LH}^2 = \omega_{ce}\omega_{ci}/(1 + \omega_{ce}^2/\omega_{pe}^2)$; however, for the parameters in Table I, one has $\omega_{ce}^2/\omega_{pe}^2 = 0.044 \ll 1$ which justifies the approximation. The depth of the striations is taken to be $n_{0,\mathrm{str}} = 0.05\, n_0 = 0.25 \times 10^{11}\ \mathrm{m}^{-3}$, which is consistent with observations (Kelley *et al.*, 1995), while the sizes of the striations and the satellite D_str and D_sat will be given a range of different values in the numerical simulations below. The satellite speed $v_\mathrm{sat} = 7.7\ \mathrm{km/s}$ is typical for an orbit altitude of about 300 km. For the charging model in Sec. IV, we will use the electron temperature $T_\mathrm{e} = 1500\ \mathrm{K}$, giving the electron Debye length $\lambda_\mathrm{De} = 0.0038\ \mathrm{m}$.

III. WAVE DISPERSION AND WAVE GENERATION BY SATELLITES

We here discuss the wave dispersion properties of the model equation (5) supporting lower hybrid, whistler and magnetosonic waves, and different wave generation mechanisms by a target satellite orbiting at a specified angle with the magnetic field lines and interacting with magnetic field aligned striations.

By assuming plane waves with $\mathbf{j}_e(\mathbf{r}, t) = \mathbf{j}_{e0}\exp(i\mathbf{k}\cdot\mathbf{r} - i\omega t)$ in Eq. (5) for homogeneous plasma $[\tilde{n}(\boldsymbol{r}_\perp) = n_0]$ and without the satellite source terms, one obtains the dispersion relation

$$\omega^2 = \left(\omega_{ce}\lambda_e^2 k^2 + \omega_{ci}\right)\frac{\omega_{ce}\lambda_e^2 k_\parallel^2 + \omega_{ci}\left(1 + \lambda_e^2 k_\perp^2\right)}{\left(1 + \lambda_e^2 k^2\right)^2}$$
$$\approx \frac{\lambda_e^2 k^2 \omega_{ce}\omega_{ci}}{\left(1 + \lambda_e^2 k^2\right)^2}\left(1 + \lambda_e^2 k^2 + \frac{\omega_{ce}}{\omega_{ci}}\lambda_e^2 k_\parallel^2\right), \tag{6}$$

where $k_\perp$ and $k_\parallel$ are the perpendicular and parallel (to the magnetic field) wave vector components, and $k = (k_\perp^2 + k_\parallel^2)^{1/2}$ is the total magnitude of the wave vector. The dispersion relation (6) is plotted in Fig. 1, where different wave modes are indicated. The dispersion relations for whistler, lower hybrid, and magnetosonic waves are obtained as limiting cases of Eq. (6). At oblique angles to the magnetic field $k_\parallel \gtrsim k_\perp$, one has the dispersion relation for whistler waves,

$$\omega^2 = \frac{\omega_{ce}^2 \lambda_e^4 k^2 k_\parallel^2}{\left(1 + \lambda_e^2 k^2\right)^2}. \tag{7}$$

In the limit of large wave vectors $\lambda_e^2 k^2 \gg 1$, the whistler wave reaches the electron cyclotron resonance $\omega^2 = \omega_{ce}^2 k_\parallel^2/k^2$. For whistlers generated by a localized source, the group velocity restricts the whistler wave to propagate within a cone of angle $\arctan\left(1/\sqrt{8}\right) = \arcsin(1/3) \approx 19.5^\circ$ to the magnetic field (Stix, 1992; Swanson, 2003). On the other hand, for perpendicular propagation to the magnetic field, $k_\parallel = 0$ and $k = k_\perp$, one has the dispersion relation for the perpendicular lower hybrid and magnetosonic waves,

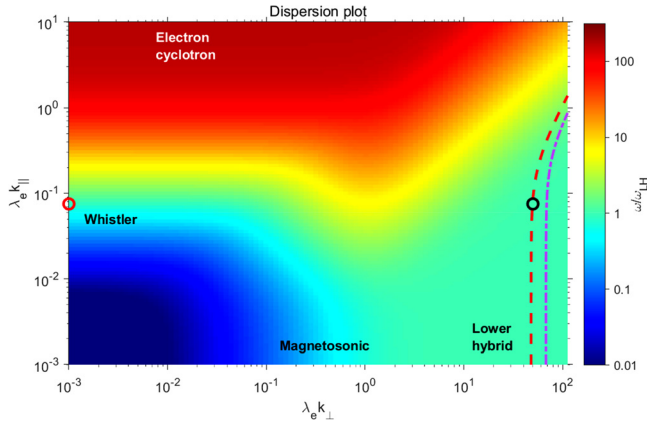

FIG. 1. Dispersion plot (logarithmic scales) showing the wave frequency ω as a function of the wave vector $(k_\perp, k_\parallel)$. Different regions of whistler, lower hybrid, and magnetosonic waves are indicated, as well as the electron cyclotron resonance. A satellite with velocity $v_\mathrm{sat} = 7.7\ \mathrm{km/s}$ can excite lower hybrid waves obeying the resonance condition (10), giving the resonant wave vectors indicated by the dashed red line for perpendicular propagation $\theta_\mathrm{sat} = \pi/2$ and the dashed–dotted purple line for oblique propagation with $\theta_\mathrm{sat} = \pi/4$. A lower hybrid wave (black circle) having the wavelength 1 m may be mode converted to a whistler wave having the same frequency and wavelength 625 m (red circle) on a magnetic field aligned striation.

$$\omega^2 = \frac{\omega_{ci}\omega_{ce}\lambda_e^2 k_\perp^2}{1+\lambda_e^2 k_\perp^2} = \frac{\omega_{LH}^2\lambda_e^2 k_\perp^2}{1+\lambda_e^2 k_\perp^2}. \quad (8)$$

In the limit of large wave vectors $\lambda_e^2 k_\perp^2 \gg 1$ one has the lower hybrid resonance $\omega^2 = \omega_{LH}^2$, while in the limit of small wave vectors $\lambda_e^2 k_\perp^2 \ll 1$, the dispersion relation supports fast magnetosonic waves $\omega^2 = \omega_{LH}^2\lambda_e^2 k_\perp^2 = v_A^2 k_\perp^2$ propagating with the Alfvén speed v_A. For short wavelengths such that $\lambda_e^2 k^2 \gg 1$, the dispersion relation (6) for obliquely propagating waves simplifies to

$$\omega^2 = \omega_{ce}\omega_{ci} + \omega_{ce}^2\frac{k_\parallel^2}{k^2} = \omega_{LH}^2 + \omega_{ce}^2\frac{k_\parallel^2}{k^2}, \quad (9)$$

encompassing both the lower hybrid and electron cyclotron resonances. Thus, the model supports the whistler, lower hybrid, and magnetosonic wave modes residing on the same dispersion surface, as shown in Fig. 1.

Next, a resonance condition for wave excitation by a satellite is derived. In the frame of a satellite propagating in the y–z plane with constant speed v_{sat} at an angle θ_{sat} to the magnetic field, in homogeneous plasma, the Doppler shifted frequency is $\omega' = \omega - \mathbf{v}_{sat}\cdot\mathbf{k} = \omega - \left(v_{sat,\perp}k_y + v_{sat,\parallel}k_z\right)$ with $v_{sat,\perp} = v_{sat}\sin(\theta_{sat})$ and $v_{sat,\parallel} = v_{sat}\cos(\theta_{sat})$. In the frame of the satellite, the Doppler shifted frequency of satellite generated waves is zero, $\omega' = 0$, so that the satellite resonantly excites waves via Cherenkov radiation obeying the resonance condition (with $k_y = k_\perp$ and $k_z = k_\parallel$),

$$\omega = v_{sat,\perp}k_\perp + v_{sat,\parallel}k_\parallel = v_{sat}\left(k_\perp\sin(\theta_{sat}) + k_\parallel\sin(\theta_{sat})\right). \quad (10)$$

By inserting the expression for ω in Eq. (10) into Eq. (6), a resonance condition connecting $k_\perp$ and $k_\parallel$ is obtained. In Fig. 1, the red dashed line indicates the resonance condition for perpendicular propagation $\theta_{sat} = \pi/2$, and the purple dashed-dotted line for oblique propagation with $\theta_{sat} = \pi/4$. As seen in Fig. 1, the satellite-generated waves in homogeneous plasma are predicted to be only electrostatic lower hybrid waves having wave vectors obeying $k_\perp^2\lambda_e^2 \gg 1$ and $k_\perp^2 \gg k_\parallel^2$. For oblique satellite propagation to the magnetic field, the perpendicular velocity $v_{sat,\perp} = v_{sat}\sin(\theta_{sat})$ is lower, leading to larger resonant lower hybrid wave vector $k_\perp$ and correspondingly shorter wavelength.

For finite $k_\parallel$, the group velocity of the satellite-generated lower hybrid waves rapidly rises in the direction perpendicular to $\mathbf{k}$ and almost parallel to $\mathbf{B}_0$. In the frame of the satellite, the group velocity of the lower hybrid waves (having $\omega' = 0$) will form a two-dimensional wedge in the y–z plane behind the satellite with parallel velocities in the range (cf. Appendix C),

$$|v_\parallel| < v_{sat,\perp}\sqrt{\frac{\omega_{ce}}{8\omega_{ci}}} = v_{sat,\perp}\sqrt{\frac{m_i}{8m_e}} \approx 60.4\,v_{sat,\perp}, \quad (11)$$

giving maximum parallel velocity of $v_\parallel = \pm 465$ km/s along the magnetic field lines of the generated lower hybrid waves for $v_{sat,\perp} = 7.7$ km/s, consistent with the simulation result in Fig. 4 below.

For finite $k_\parallel$ lower hybrid waves, as shown in Fig. 2, the frequency rises rapidly from the lower hybrid frequency $f = (f_{ce}f_{ci})^{1/2}$ and transitions to the electron cyclotron resonance $f = f_{ce}\cos\theta$, where $\cos\theta = k_\parallel^2/k^2$ describes the angle of the wave vector to the magnetic field [cf. Eq. (9)]. In the limit of small wavenumbers, the lower hybrid wave becomes electromagnetic and connects to the fast magnetosonic wave

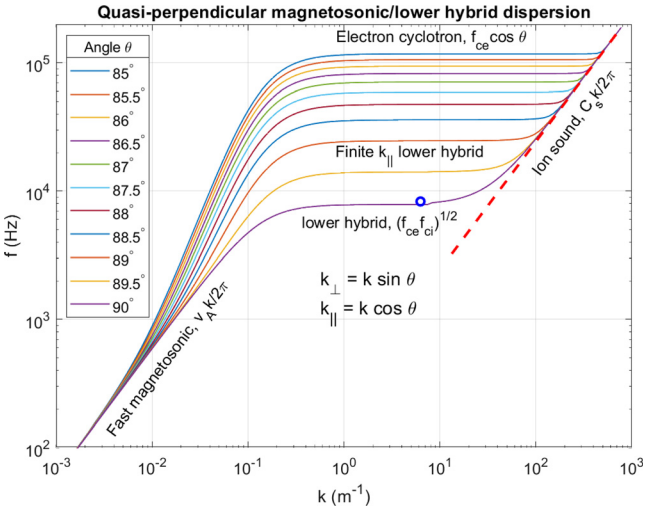

FIG. 2. Dispersion curves for frequency $f = \omega/2\pi$ vs wavenumber k for quasi-perpendicular magnetosonic and lower hybrid waves for different angles θ of the wave vector to the magnetic field. The blue ring indicates the typical wavenumber and frequency of satellite-generated lower hybrid waves. The dispersion curves were obtained from the cold plasma dispersion relation (6) for $k \le 8\,\mathrm{m}^{-1}$ and from the electrostatic dispersion relation (D7) in Appendix D for $k > 8\,\mathrm{m}^{-1}$ including thermal effects. The red dashed line indicates the ion sound speed $C_s = 1.5$ km/s.

with frequency $f = v_A k/2\pi$. Typical lower hybrid waves generated by a satellite, indicated by a blue ring in Fig. 2, are electrostatic with a wavelength of about 1 m and a frequency close to the lower hybrid frequency. The high-k limit of validity of the present cold plasma model is reached when the frequency of the ion sound speed $C_s \sim 1.5$ km/s becomes comparable to or exceeds the phase speed ω/k of the cold plasma wave (cf. Appendix D).

In the presence of small-scale magnetic field aligned striations, a lower hybrid wave having its wave vector nearly perpendicular to the striation (black circle in Fig. 1) may be mode converted to a whistler wave propagating almost parallel to the striation (red circle), with the whistler wave having the same frequency as the lower hybrid wave.

It was empirically found by Eliasson and Papadopoulos (2008) that optimal mode conversion efficiency between lower hybrid and whistler waves propagating parallel to the magnetic field occurs when the lower hybrid wavenumber k_{LH} and striation width D_{str} are related through (see Fig. 3)

$$k_{LH}D_{str} \approx 1.5. \quad (12)$$

A satellite with velocity $v_{sat,\perp}$ propagating perpendicularly to the magnetic field will generate a wake of lower hybrid waves having the wavelength $\lambda_{LH} \approx v_{sat,\perp}/f_{LH}$ and wave vector $k_{LH} \approx 2\pi/\lambda_{LH}$, which from Eq. (12) gives the optimal striation width

$$D_{str,\,opt} \approx 0.25\frac{V_{sat,\perp}}{f_{LH}}, \quad (13)$$

for mode conversion of satellite-generated lower hybrid waves to whistler waves; hence, the optimal striation width will be $D_{str,\,opt} \approx 0.25$ m for a satellite having velocity $V_{sat,\perp} = 7.7$ km/s perpendicular to the magnetic field.

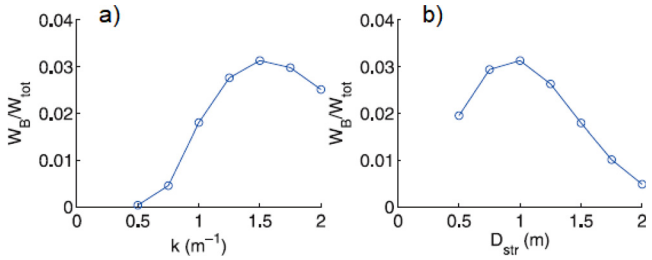

FIG. 3. Efficiency of whistler wave generation (fraction of whistler energy W_B to total wave energy W_{tot}) as a function (a) of k_{LH} for $D_{str} = 1$ m and (b) of D_{str} for $k_{LH} = 1.5\,m^{-1}$. Reproduced with permission from B. Eliasson and K. Papadopoulos, J. Geophys. Res. **113**, A09315 (2008). Copyright 2008 by the American Geophysical Union.

The condition (12) agrees well with that of Camporeale *et al.* (2012) who theoretically derived a maximum mode conversion efficiency for $k_{LH}D_{str} = \sqrt{2} \approx 1.4$ for the general case of oblique whistler propagation. A similar condition was derived by Bell and Ngo (1990) for the mode conversion process of electromagnetic whistlers to lower hybrid waves. Laboratory experiments of the interaction of whistler and lower hybrid waves with striations have been carried out at the UCLA Large Plasma Device (Bamber *et al.* 1994; 1995; Rosenberg and Gekelman 1998; 2000; 2001).

The satellite may also directly generate pulses of whistler and magnetosonic waves while traversing and interacting with the striation. This mechanism will generate a modulated wave pulse with broad frequency spectrum and does not rely on the intermediate generation of lower hybrid waves by the satellite. When the satellite traverses the striation, the interaction time increases with the width of the striation and the size of the satellite but decreases for higher satellite velocities transverse to the striation. Therefore, the frequency spectrum of the generated waves can be expected to have a peak amplitude at a frequency f_{peak} proportional to the transverse satellite velocity but inversely proportional to the sum of widths of the satellite and striation. The empirical formula

$$f_{peak} = \frac{0.4\, v_{sat,\perp}}{D_{sat} + D_{str}} \tag{14}$$

is consistent with the spectral peaks obtained numerically in Sec. V D.

The generation of shear Alfvén waves is not considered in the present model due to their low frequency ($\omega < \omega_{ci}$) and long wavelength ($\lambda_A > 2\pi\lambda_i \sim 8$ km) compared to typical object sizes. However, by including the Lorenz force of the magnetic field on the ions in Eq. (1), there could be possibility of a satellite to generate shear Alfvén waves propagating parallel to the magnetic field lines (Bernhardt *et al.*, 2023) with dispersion relation $\omega^2 = v_A^2 k_\parallel^2$.

Also, because the ionosphere is a low temperature plasma, the electron and ion thermal pressures have been neglected in the present cold plasma wave model. This excludes for example the ion-acoustic wave which has a wave speed of about 1.5 km/s and could form a Mach cone behind the satellite. However, because of almost equal electron and ion temperatures, $T_e \sim T_i$, the ion-acoustic wave are heavily Landau damped [see, e.g., Chen (1984), Figs. 7–31], preventing it from propagating far away from the satellite or space debris that generated it. Ion-acoustic solitons (Tran, 1979) were observed in the laboratory (Ikezi *et al.*, 1970; Saitou and Nakamura, 2005), when it became possible to produce plasma with hot electrons and cold ions ($T_e \gtrsim 10T_i$) to reduce the effects of ion Landau damping and reflection of low-energy ions by the solitary wave. The ion-acoustic solitons are characterized by a localized density hump with a positive potential, have velocities slightly above the linear ion-acoustic speed, and have typical widths of a few Debye lengths, i.e., a few centimeter for ionospheric conditions. The dispersion effect enabling the solitons comes the deviation from exact charge neutrality at Debye length scale, which balances the nonlinearities of the system. Early theoretical models of ion and electron Landau damping of nonlinear ion-acoustic were developed by Taniuti (1972), VanDam and Taniuti (1973), and Ott and Sudan (1969). Because of strong ion Landau damping at ionospheric conditions with $T_e \sim T_i$, Debye length-sized ion-acoustic solitons will not propagate far from the space debris at low earth orbit (LEO) and may be hard to detect *in situ* or with radars (Bernhardt *et al.*, 2023). It should be noted that simplified formulas of ion Landau damping are commonly derived under the condition that $T_e \gg T_i$ [e.g., McKinstrie *et al.* (1999)] and may strongly under-estimate the damping rate and, therefore, over-estimate the longevity of ion acoustic solitons launched by hypersonic space objects [e.g., Truitt and Hartzell (2020b)] when the electron and ion temperatures are comparable (cf. Appendix A). Ion phase-space holes have been observed in space near the bow shock (Wang *et al.*, 2020) and in the laboratory (Pécseli *et al.*, 1981; 1984), when $T_e \gtrsim 3T_i$, consistent with the theoretically predicted condition $T_e > 3.5T_i$ for the existence of solitary ion holes (Schamel and Bujarbarua, 1980; Bujarbarua and Schamel, 1981). The ion holes are characterized by a localized density reduction with a negative potential that traps a portion of ions, a bipolar electric field, and have speeds near or below the ion thermal speed. Even though ion holes could possibly be formed by space debris when $T_e \gtrsim 3T_i$, they are not supported in the present cold fluid model.

IV. SATELLITE CHARGING ESTIMATE

A simplified model based on spherical symmetry is used to estimate the charges attached to satellites of different sizes. The ion thermal speed is of the order 1 km/s which is much lower than the satellite/space debris speed 7.7 km/s, and the ions will impact the satellite with straight ballistic orbits at the ram side, while there may be a wake of lower plasma density on the opposite side. This leads to the ion current [e.g., Anderson (2012)]

$$I_i = en_0\pi R^2 v_{sat}. \tag{15}$$

On the other hand, the typical thermal speed of the electrons in the ionosphere is 150 km/s, which is much higher than the satellite/space debris speed. Therefore, the electrons may be assumed to be at thermal equilibrium around the satellite, and the current due to the fast electrons hitting the satellite from all sides is

$$I_e = -en_0\pi R^2 \sqrt{\frac{8k_B T_e}{\pi m_e}} \exp\left(\frac{e\phi_0}{k_B T_e}\right), \tag{16}$$

where the effect of the electron repulsion by the negative potential is considered in the exponential factor for the Boltzmann distributed electron density. Setting $I_i + I_e = 0$ leads to a typical negative floating potential of less than a Volt. However, satellites in polar orbits can acquire a few orders of magnitude higher voltages during intense

electron precipitation events (Anderson, 2012), leading to a significant increase in the electron current to the satellite compared to Eq. (16) due to the bombardment of the satellite by accelerated electrons having energies exceeding the negative potential barrier. At high altitudes and low plasma density, the satellite may become positively charged by emitting photoelectrons due to UV irradiation and when sunlit (Whipple, 1981).

For a given satellite potential ϕ_0 relative to the surrounding plasma, the charge state depends on the satellite size and how the plasma forms a sheath around the satellite. In vacuum, a negatively charged sphere of radius R and surface potential ϕ_0 has charges residing on the surface, with the total charge

$$Q = Q_{\rm vac} = C\phi_0, \tag{17}$$

with capacitance $C = 4\pi\epsilon_0 R$. In stationary plasma, a cloud of opposite charges surrounds the sphere, leading to Debye shielding and rapid decrease in the potential. For a small sphere, $R < \lambda_{\rm De}$ where $\lambda_{\rm De}$ is the electron Debye length (cf. Table I), the Debye–Hückel potential (for $r > R$) is

$$\phi = \phi_0 \frac{R}{r} e^{-(r-R)/\lambda_{\rm De}}, \tag{18}$$

and which is valid for small potentials, $|e\phi| \ll k_B T_e$. The electric field is

$$\mathbf{E} = -\nabla\phi = \phi_0 R\left(\frac{1}{r^2} + \frac{1}{r\lambda_{\rm De}}\right) e^{-(r-R)/\lambda_{De}}\,\hat{\mathbf{r}}, \tag{19}$$

where $\hat{\mathbf{r}}$ is the unit vector pointing radially outwards. Gauss' law on integral form gives the charge Q enclosed within a sphere with radius $r > R$ as an integral over the sphere's surface S,

$$\begin{aligned} Q = \epsilon_o \oiint_S \mathbf{E}\cdot \mathrm{d}\mathbf{S} &= \epsilon_0\phi_0 R\left(\frac{1}{r^2} + \frac{1}{r\lambda_{De}}\right) e^{-(r-R)/\lambda_{De}} \underbrace{\oiint_S \mathrm{d}S}_{=4\pi r^2} \\ &= 4\pi\epsilon_0\phi_0 R\left(1 + \frac{r}{\lambda_{De}}\right) e^{-(r-R)/\lambda_{De}}, \end{aligned} \tag{20}$$

where it was used that the differential surface element points radially outwards, $d\mathbf{S} = \hat{\mathbf{r}}\mathrm{d}S$ and that the surface area of the sphere is $S = 4\pi r^2$. The charge contained inside the sphere, as $r \to R$, is

$$Q = Q_{\rm Debye} = 4\pi\epsilon_0\phi_0 R\left(1 + \frac{R}{\lambda_{De}}\right) = Q_{\rm vac}\left(1 + \frac{R}{\lambda_{De}}\right), \tag{21}$$

which equals the surface charge of the spherical object. Hence, the capacitance is a factor $(1 + R/\lambda_{De})$ larger in plasma compared to the vacuum case due to the Debye sheath of thickness λ_{De}. However, for a larger sphere, $R > \lambda_{De}$ and nonlinearly large negative potentials, $|e\phi| \gg k_B T_e$, the sheath forms an ion-rich region depleted of electrons due to the Boltzmann factor $\exp(e\phi/k_B T_e)$ in the electron number density. In this case, the spherical object may work as a capacitor with a potential-dependent electron density gap between the surface and the surrounding plasma—a larger gap gives a smaller capacitance, similar to regular capacitors. The ion density is also modified by the potential, but to lesser extent due to their large mass. As an estimate, we use an analytic function fit by Blackwell *et al.* (2005) to numerical calculations by Laframboise (1966) of the sheath thickness s, given by

$$s = \left(2.5 - 1.87e^{-0.3R/\lambda_{De}}\right)\left(-\frac{e\phi_0}{k_B T_e}\right)^{2/5}\lambda_{\rm De}, \tag{22}$$

which is valid for negative potentials. Using s in place of $\lambda_{\rm De}$ in Eq. (19) gives

$$Q = Q_{\rm sat} = 4\pi\epsilon_0\phi_0 R\left(1 + \frac{R}{s}\right) = Q_{\rm vac}\left(1 + \frac{R}{s}\right), \tag{23}$$

as an estimate of the charge [e.g., Manchester (2010)], with values in between $Q_{\rm vac}$ and $Q_{\rm Debye}$. Hence, the scaling of the satellite charge with size depends on the radius compared to the Debye length: For macroscopic objects much larger than the Debye length, the charge scales with the surface area $Q \propto R^2$ while for very small objects the scaling is $Q \propto R$.

We consider conditions at HAARP which is in the polar region and may have some degree of electron precipitation and increased electron attachment on the satellite and a moderately high surface potential $\phi_0 = -8$ V, and will calculate the satellite charge from Eqs. (22) and (23). For example, a radius $R = 0.5$ m, with $T_e = 1500$ K and $\lambda_{\rm De} = 0.0038$ m gives $s \approx 13\lambda_{\rm De}$ and an estimated satellite charge $Q_{\rm sat} = -5$ nC. This is one order of magnitude larger than the vacuum estimate but an order of magnitude smaller than the Debye sheath estimate.

V. SIMULATIONS OF WAVE GENERATION BY SATELLITE AND STRIATION INTERACTIONS

A set of simulations of Eq. (5) are carried out to investigate the generation of lower hybrid, whistler and magnetosonic waves by satellites traversing and interacting with striations and how the striation width and satellite size impacts the generation of different wave modes. The frequency spectra of the generated wave modes are analyzed. The wave dispersive properties in combination with the Poynting flux may be used to estimate the distance and direction to the space debris.

A. Computational model

In the numerical simulations, a two-dimensional (2D) geometry is used in the y–z plane with periodic boundary conditions, in which the magnetic field is directed parallel to the z axis, and the satellite is propagating along the y axis, perpendicular to the magnetic field. For computational efficiency, the surface charge of the satellite is represented as a localized "cloud" of charges, using a 2D Gaussian profile of the charge density, of the following form:

$$\rho_{\rm sat}(\boldsymbol{\xi}) = \rho_{0\rm sat}\exp\left(-\frac{(y - v_{\rm sat}t)^2}{D_{\rm sat}^2} - \frac{z^2}{D_{\rm sat,\|}^2}\right), \tag{24}$$

which for computational efficiency uses an artificially elongated profile $D_{\rm sat,\|} = 100$ m along the z axis. To ensure that the charge density in Eq. (24) corresponds to a total charge $Q_{\rm sat}$, we temporarily extend $\rho_{\rm sat}$ to 3D, and require that

$$\begin{aligned} Q_{\rm sat} &= \iiint \rho_{0\rm sat}\exp\left(-\frac{x^2}{D_{\rm sat}^2} - \frac{(y - v_{\rm sat}t)^2}{D_{\rm sat}^2} - \frac{z^2}{D_{\rm sat,\|}^2}\right) dx\,dy\,dz \\ &= \pi^{3/2} D_{\rm sat}^2 D_{\rm sat,\|}, \end{aligned} \tag{25}$$

giving the model charge density $\rho_{0\rm sat} = Q_{\rm sat}/\left(\pi^{3/2} D_{\rm sat}^2 D_{\rm sat,\|}\right)$ to be used in Eq. (22).

The variables in the wave equation (5) are represented on a 2D rectangular domain in the y–z plane of sizes $-2\,\mathrm{km} < y < 2\,\mathrm{km}$ and $-10\,\mathrm{km} < z < 10\,\mathrm{km}$ and are resolved on a numerical grid with periodic boundary conditions in both directions. Numerical details and parameters are given in Appendix E.

In the analysis of the numerical results, the wave electric and magnetic fields $\mathbf{E}$ and $\mathbf{B}$ are calculated from the solution $\mathbf{j}_{e1}$ using the following formulas:

$$\left(1-\lambda_e^2\nabla^2\right)\mathbf{E} \cong \frac{\lambda_e^2\mathbf{V}[\mathbf{V}\cdot(\mathbf{j}_{e1}\times\mathbf{B}_0)]}{n_0} - \frac{\mathbf{j}_{e1}\times\mathbf{B}_0}{n_0} \tag{26}$$

and

$$\nabla^2\mathbf{B} = \mu_0 e\mathbf{V}\times\mathbf{j}_{e1} \tag{27}$$

with the space derivatives calculated in Fourier space ($\mathbf{V}\to i\mathbf{k}$, $\nabla^2\to -k^2$).

B. Cherenkov radiation of lower hybrid waves by satellites

Simulations are carried out with a satellite propagating with velocity $v_{sat} = 7.7$ km/s along the y axis, perpendicular to the magnetic field directed along the z axis. The satellite charge is estimated from Eqs. (22) and (23) by using the satellite size $R = D_{sat}$ and the potential $\phi_0 = -8$ V. Table II shows the satellite charges for different satellite sizes used in the numerical study, as well as the amplitudes of the generated lower hybrid waves 20 m behind the satellite, as discussed below.

Figure 4 shows lower hybrid waves generated by a satellite of size $D_{sat} = 0.25$ m. It is seen that a wake of lower hybrid waves is formed behind the satellite via Cherenkov radiation, having the wavelength $\lambda_{LH} = V_{sat}/f_{LH} \approx 1$ m, and spreading along the magnetic field with a parallel group velocity consistent with Eq. (11). There is no generation of whistler or magnetosonic waves by the satellite, in agreement with the resonance condition in Eq. (10) shown as a dashed red line in Fig. 1. The amplitude of the lower hybrid waves behind the satellite decreases approximately as $1/\sqrt{r}$ with distance r away from the satellite.

Comparisons of the lower hybrid wave electric field amplitudes E_y (cf. Fig. 4) measured at 20 m behind the satellite for different satellite sizes are listed in Table II. While the satellite charge increases with increasing satellite size, the generation of lower hybrid waves is most efficient for satellites of $D_{sat} \approx 0.1$–0.25 m. Smaller satellites have lower charge states due to their smaller surface area leading to a decrease in the amplitude of the generated lower hybrid waves. Larger satellites may generate lower hybrid waves less efficiently, despite their higher charge states, when their size becomes comparable to the lower hybrid wavelength. This can be understood in that the lower hybrid waves have a certain wavelength λ_{LH} which has to be driven resonantly in order to be excited. The charge density of the satellite in a frame moving with the satellite is of the following form: $\rho_{sat}(\boldsymbol{\xi}) = \rho_{0,sat}\exp\left(-\xi^2/D_{sat}^2\right)$. If we assume a simple 1D model, with $\xi = \xi_x$, the charge density in Fourier space is given by $\hat{\rho}_{sat}(k) = \sqrt{\pi}\rho_{0,sat}D_{sat}\exp\left(-D_{sat}^2k^2/4\right)$. The resonant wave number for driving the lower hybrid wave is $k = k_{LH} = 2\pi/\lambda_{LH}$, where $\lambda_{LH} \approx 1$ m is the wavelength of the lower hybrid wave, and the resonant source is $\hat{\rho}_{sat}(k_{LH}) = \sqrt{\pi}\rho_{0,sat}D_{sat}\exp\left(-D_{sat}^2k_{LH}^2/4\right) = \sqrt{\pi}\rho_{0,sat}D_{sat}\exp\left(-\pi^2D_{sat}^2/\lambda_{LH}^2\right)$. Hence, we can see that the source term decreases exponentially when the satellite size becomes comparable or larger than the LH wavelength. For example, for $D_{sat} = 0.1$ m $= 0.1\lambda_{LH}$ we have $D_{sat}\exp\left(-\pi^2D_{sat}^2/\lambda_{LH}^2\right) \approx 0.1$ m while for $D_{sat} = 1$ m $= \lambda_{LH}$, we have $D_{sat}\exp\left(-\pi^2D_{sat}^2/\lambda_{LH}^2\right) \approx 5\times10^{-5}$ m, i.e., more than 3 orders of magnitude smaller than for $D_{sat} = 0.1$ m. This explains the low amplitude of the LH field for $D_{sat} = 1$ m in Table II.

TABLE II. The satellite charge Q_{sat} for different sizes D_{sat} assuming the satellite potential $\phi_0 = -8$ V, and the amplitude $|E_y|$ of the satellite-generated lower hybrid (LH) wave, 20 m behind the satellite.

D_{sat} (m)	Q_{sat} (nC)	LH field $\lvert E_y\rvert$ (mV/m)
0.05	−0.090	4
0.1	−0.27	8
0.25	−1.35	7
0.5	−5.0	2
1	−19.0	10^{-3}

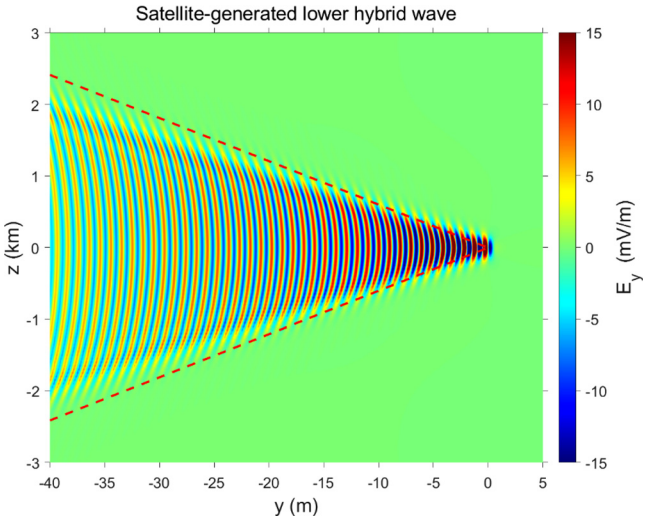

FIG. 4. Simulation of a satellite of size $D_{sat} = 0.25$ m propagating from left to right and generating lower hybrid (LH) waves of wavelength $\lambda_{LH} = v_{sat}/f_{LH} \approx 1$ m forming a wedge in the y–z plane behind the satellite, here located at $y = z = 0$. The lower hybrid waves spread along the magnetic field lines with velocity $|v_\parallel| = |v_z| < 465$ km/s for satellite velocity $v_{sat} = 7.7$ km/s [dashed red lines; cf. Eq. (11)]. For clarity to visualize the very different length scales, the y axis is enhanced and covers 45 m, while the z axis covers 6 km.

C. Excitation of whistler and magnetosonic waves on magnetic field aligned irregularities

Magnetic field aligned irregularities (striations) can work as scattering centers to generate whistler and magnetosonic waves when interacting with satellites and satellite-generated lower hybrid waves. An overview of the results are shown in Table III, where it is seen that LH-whistler mode conversion is most efficient for small striations and

TABLE III. The generation of whistler and magnetosonic waves by satellites and striations of different sizes showing the amplitude of the generated waves at a distance from the target parallel and perpendicular to the magnetic field, and the generation mechanisms through LH-whistler mode conversion and direct satellite-striation interaction. Figures showing the wave forms are indicated where available.

D_{sat} (m)	D_{str} (m)	Wave mode	Amplitude (pT)	Distance	Generation mechanism	Figure
0.05	0.05	Whistler	0.01	3 km ∥ **B**	LH-whistler	Not shown
0.1	0.1	Whistler	0.02	3 km ∥ **B**	LH-whistler	Not shown
0.1	0.25	Whistler	0.02	3 km ∥ **B**	LH-whistler	Not shown
0.25	0.25	Whistler	0.03	3 km ∥ **B**	LH-whistler	Figure 5
0.5	0.5	Whistler	0.000 5	5 km ∥ **B**	LH-whistler	Figure 11
0.5	0.5	Whistler	0.008	5 km ∥ **B**	Sat.-striation	Figures 11 and 14
0.5	0.5	Magnetosonic	0.000 25	1 km⊥**B**	Sat-striation	Figure 12
0.5	1	Whistler	0.008	3 km ∥ **B**	Sat.-striation	Figure 6
1	4	Whistler	0.003	3 km ∥ **B**	Sat.-striation	Figure 7
1	4	Magnetosonic	0.001	0.8 km⊥**B**	Sat.-striation	Figure 7

satellites, while satellite-striation interaction is more efficient for larger sizes, as discussed below.

For small-scale striations of width $D_{str} = 0.5$ m or less, an important generation mechanism is the mode conversion of satellite-generated lower hybrid waves to whistler waves, with an optimal striation width $D_{str} = 0.25$ m for mode conversion as given by Eq. (13). Figure 5 shows a simulation for the optimal striation width $D_{str} = 0.25$ m and near-optimal satellite size $D_{sat} = 0.25$ m (cf. Table II) for the generation of lower hybrid waves. The satellite generates lower hybrid waves which continuously mode convert to whistler waves after the satellite has crossed the striation. The whistler waves have wave vectors ranging from parallel to nearly perpendicular to the magnetic field lines, but their propagation (group velocity) is confined within the cone of $\sim 19.5°$ to the magnetic field. The interaction between the satellite and striation also generates modulated pulses of whistlers and dispersive magnetosonic waves, not visible in Fig. 5 but discussed in Sec. V E.

For striations of widths $D_{str} > 0.5$ m, the mode conversion of satellite-generated lower hybrid waves to whistler waves becomes increasingly inefficient, and the main mechanism is through direct interaction between the satellite and the striation. Figure 6 shows a simulation with the width $D_{str} = 1$ m [Fig. 6(b)] and satellite size $D_{sat} = 0.5$ m. The satellite generates a wake of lower hybrid waves [Fig. 6(a)] as well as a modulated pulse of long wavelength whistler waves [Figs. 6(c) and 6(d)], but there is no visible mode conversion of the satellite-generated lower hybrid waves to whistler waves after that the satellite has traversed the striation. Also here, the whistler waves are confined within a cone of $\sim 19.5°$ to the background magnetic field. The amplitudes of the satellite-generated whistler waves in Figs. 6(c) and 6(d) are about an order of magnitude lower compared to that of the mode converted whistlers in Figs. 5(c) and 5(d).

Finally, a simulation is carried out for a larger scale striation of $D_{str} = 4$ m and a satellite of size $D_{sat} = 1$ m, shown in Fig. 7. The satellite interacts with the striations to generate a modulated whistler pulse of longer wavelength and lower amplitude propagating within a cone to the magnetic field lines. In addition, a magnetosonic wave pulse is generated [Fig. 7(d)] which propagates nearly perpendicular to the magnetic field lines. It is located at $y \sim 0.7$ km at $t = 1.5$ ms, corresponding to a speed of ~ 470 km/s, somewhat higher than the Alfvén speed $v_A = 370$ km/s. In general, larger striations and larger satellites interacting with them, generate whistler waves with longer wavelengths corresponding to lower frequencies, as will be discussed in Sec. V D.

D. Frequency spectra of satellite-generated waves

Here, the frequency spectra of satellite-generated waves are investigated, motivated by observations of waves generated during conjunctions of satellites. Figure 8 shows the recorded signal during a conjunction between the Swarm-E/Enhanced Polar Outflow Probe (e-POP) and Starlink 2521 spacecraft (Bernhardt *et al.*, 2023), where a burst of waves (denoted a FLASH event) was observed, and where the frequency spectrum of the waves ranged from the ion cyclotron frequency up to the lower hybrid frequency.

TABLE IV. Target properties from plasma wave observations.

Property	Direction of target emission	Distance along $\mathbf{B}_0$ to plasma wave emitter	Distance across $\mathbf{B}_0$ to plasma wave emitter
Instrument	Low frequency vector sensor	Plasma wave receiver	Plasma wave receiver
Measurement	Electric and magnetic fields	Plasma wave complex fields	Plasma wave complex fields
Derived quantity	Poynting flux vector	Whistler frequency and drift	Magnetosonic wave frequency and drift
Application formula	$\langle \mathbf{S} \rangle = \frac{\langle \mathbf{E} \times \mathbf{B} \rangle}{\mu_0}$	$L_{\parallel} = 4\lambda_e \frac{-\omega_{ce}^2}{\dot{\omega}(t)} \left(\frac{\omega(t)}{\omega_{ce}} \right)^{3/2}$	$L_{\perp} = \frac{\omega_{LH} v_A}{3\dot{\omega}(t)} \frac{\omega_{LH}}{\omega(t)} \left(1 - \frac{\omega^2(t)}{\omega_{LH}^2} \right)^{5/2}$

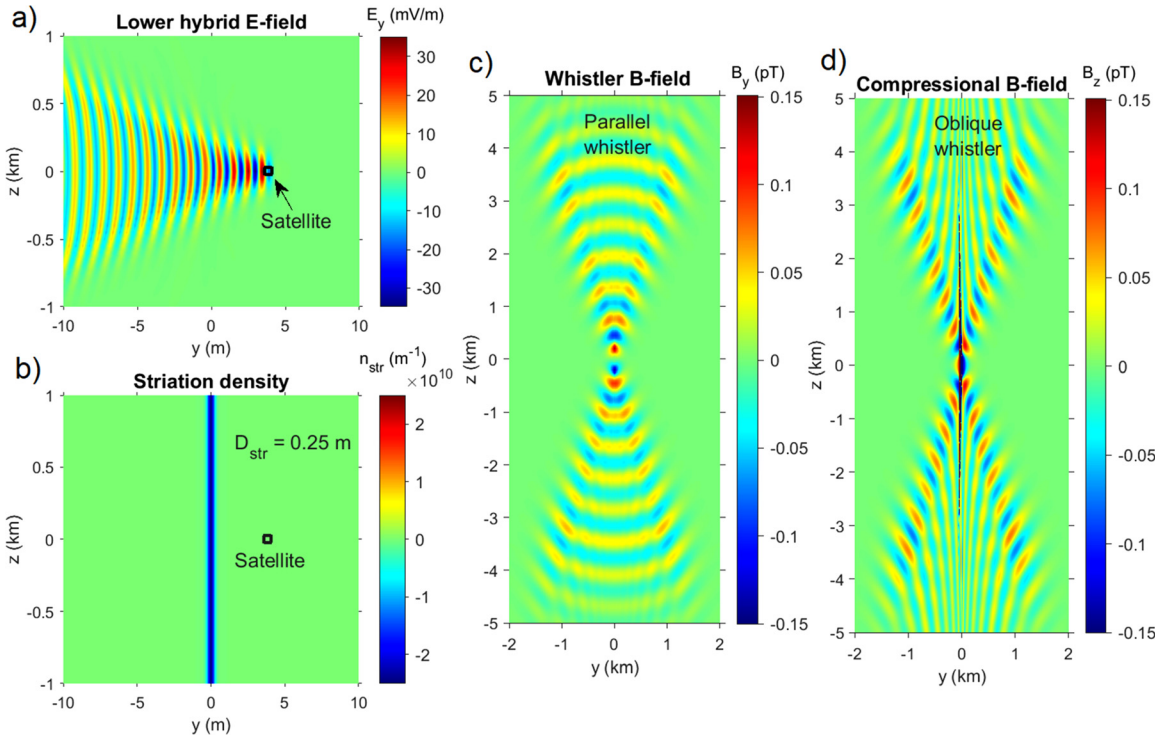

FIG. 5. Simulation of a satellite of size $D_{sat} = 0.25$ m crossing a supersmall-scale striation of width $D_{str} = 0.25$ m at time $t = 0$. At $t = 0.5$ ms, satellite-generated lower hybrid waves [panel (a)] are being mode converted on the striation [panel (b)] to generate parallel and oblique whistler waves [panels (c) and (d)].

To compare with the observations, the simulated wave field is recorded at a few different locations near the satellite that is crossing a striation. Figures 9 and 10 show the simulation results for a satellite of size $D_{sat} = 0.5$ m which is crossing striations of widths $D_{str} = 0.5$, 1, 2, and 4 m. The frequency spectra are calculated at different locations along and perpendicular to the background magnetic field. Along the magnetic field lines from the satellite (Fig. 9), the wave component B_y is measured, associated with whistler waves, while perpendicular to the magnetic field from the satellite (Fig. 10) the compressional wave component B_z is measured, associated with both oblique whistlers and magnetosonic/lower hybrid waves.

The frequency spectra in Fig. 9 of whistlers propagating along the magnetic field lines contain low frequency components that are strongly dependent on the striation width D_{str}, with spectral peaks at lower frequencies for larger D_{str}. These broad frequency components are associated with the satellite interacting directly with the striation to generate modulated pulses of whistler waves (cf. Figs. 6 and 7), giving intensity maxima at frequencies consistent with the formula for f_{peak} in Eq. (14); for example, it is seen in Fig. 9 that $D_{str} = 0.5$ and 4 m have intensity maxima at $f \approx 3$ and 0.6 kHz, consistent with formula (14) giving $f_{peak} = 3.1$ and 0.7 kHz, respectively.

A narrow spectral peak is also seen slightly above the lower hybrid frequency for the smallest striation $D_{str} = 0.5$ m and at an order of magnitude lower intensity for $D_{str} = 1$ m. These peaks are associated with satellite-generated lower hybrid waves converting to whistler waves on the striation (see, e.g., Fig. 5), as discussed in Sec. III. The small but finite parallel wave vectors of the lower hybrid waves lead to the slight upshift in frequency of the peaks compared to the lower hybrid resonance frequency $f_{LH} = 7.87$ kHz indicated with vertical dashed red lines. The spectra at different distances from the satellite, at $z = 1$ and 5 km, are similar except for an attenuation by a factor 5 consistent with the 2D geometry giving a $1/r$ dependence of the intensity with distance r from the satellite; in 3D the attenuation is expected to have a $1/r^2$ dependence due to conservation of energy.

Figure 10 shows the frequency spectra of the compressional wave component B_z at different distances from the satellite in the direction perpendicular to the background magnetic field. The spectra at $y = 0.2$ km are similar to the ones in Fig. 9 and may be associated with the near-field of oblique whistler waves. Also, here there are broad low frequency component depending on the striation width, as well as sharp peaks slightly above the lower hybrid frequency for the smallest striations $D_{str} = 0.5$ and 1 m. However, 1 km away from the satellite, the intensity has decreased about 2 orders of magnitude. The lowest frequency components below 0.5 kHz may be associated with magnetosonic waves propagating perpendicular to the background magnetic field.

We note, however, that even though the frequency spectra obtained in the simulations are consistent with the e-POP observations in Fig. 8, the amplitudes of the simulated whistler and magnetosonic waves are too low to account for the observed amplitude ~ 0.3 mV in Fig. 8. The radio receiver instrument (RRI) on e-POP (James *et al.*, 2015) consists of four 3 m monopoles organized as two crossed dipoles (channels A and B). The observed amplitude 0.3 mV in Fig. 8 would correspond to a wave electric field ~ 0.1 mV/m if one assumes an

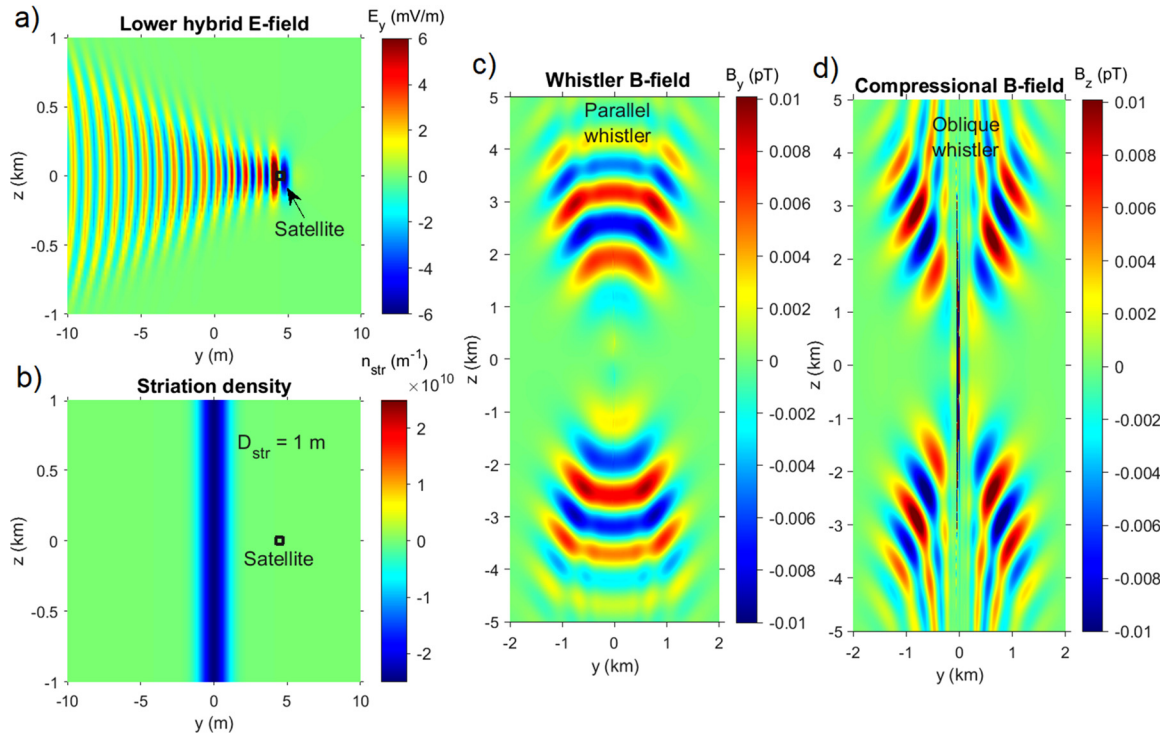

FIG. 6. Simulation of a satellite of size $D_{sat} = 0.5$ m crossing a striation of width $D_{str} = 1$ m at time $t = 0$. At $t = 0.58$ ms, the satellite [panel (a)] has interacted with the striation [panel (b)] to generate a long wavelength pulse of parallel and oblique whistler waves [panels (c) and (d)]. No mode conversion of lower hybrid waves to whistlers is visible.

effective antenna length 3 m. In the simulations, the amplitudes of the wave magnetic field and induced electric field are roughly related through Faraday's law as $E = v_{ph}B$, where $v_{ph} = \omega/k$ is the phase velocity. For parallel propagating whistlers, the phase velocity is $v_{ph} \approx 5 \times 10^6$ m/s for frequencies near the lower hybrid frequency, while dispersive magnetosonic waves propagating perpendicular to the magnetic field have phase velocities below the Alfvén speed 3.7×10^5 m/s. For the whistler wave magnetic field 0.03 pT in Fig. 5, the induced electric field is about 0.15 μV/m, much below the observed amplitude in Fig. 8. Running the RRI preamplifier on high gain would give a lower signal threshold amplitude 0.3 μV rms and assuming an effective antenna length 3 m this would give a threshold electric field 0.1 μV/m rms which could potentially measure the wave electric field 0.15 μV/m. However, during the observation in Fig. 8, the RRI was run using medium gain with a threshold amplitude 10 μV rms corresponding to about 3 μV/m rms, which is a threshold above the expected amplitude for the whistler and magnetosonic waves in the simulations. Further comments and possible mechanisms for the observations are given in the conclusions.

E. Detection and localization of space debris via wave dispersion delay and Poynting flux

The dispersive properties of whistler and magnetosonic waves may enable to estimate the distance to the satellite or space debris crossing a striation, and the direction may be found via the Poynting flux of the wave. The distance calculation is analogous to the method in astrophysics of finding the distance to pulsars using the dispersion delay of radio waves (Lorimer and Kramer, 2005). When short pulses are generated by the satellite crossing a striation, waves with different frequencies will propagate with different group velocities and will reach a receiver on board a nearby spacecraft at different times, resulting in a frequency-chirped received signal. A classic example is whistlers generated by thunderstorms (Fiser *et al.*, 2010), which have a characteristic descending tone in the kiloHertz range (Helliwell, 1965). Figure 11 shows a spectrogram for the case of a satellite of size $D_{sat} = 0.5$ m crossing a small striation of width $D_{str} = 0.5$ m. The spectrogram has two components, namely, a large amplitude pulse with descending frequency generated by satellite-striation interaction and a sustained signal near the lower hybrid frequency 7.87 kHz due to the conversion of satellite-generated lower hybrid waves to whistlers on the striation.

The slope of the whistler signal with time can be used to estimate the distance to the satellite in the following way. The dispersion relation (6) for parallel propagating whistler waves gives $\omega = \lambda_e^2 k_\parallel^2 \omega_{ce}$ for $\lambda_e^2 k_\parallel^2 \ll 1$, and the corresponding wave vector $k_\parallel = \lambda_e^{-1}\sqrt{\omega/\omega_{ce}}$. The time for a whistler wave created at time $t = t_0$ to propagate a distance L is $t - t_0 = L/v_g$ where the whistler group velocity

$$v_g = \frac{\partial \omega}{\partial k_\parallel} = 2\lambda_e^2 k_\parallel \omega_{ce} = 2\lambda_e \sqrt{\frac{\omega}{\omega_{ce}}}\omega_{ce}, \tag{28}$$

where it is seen that higher ω propagate with higher group velocity. Hence, the time taken for the whistler to propagate a distance L,

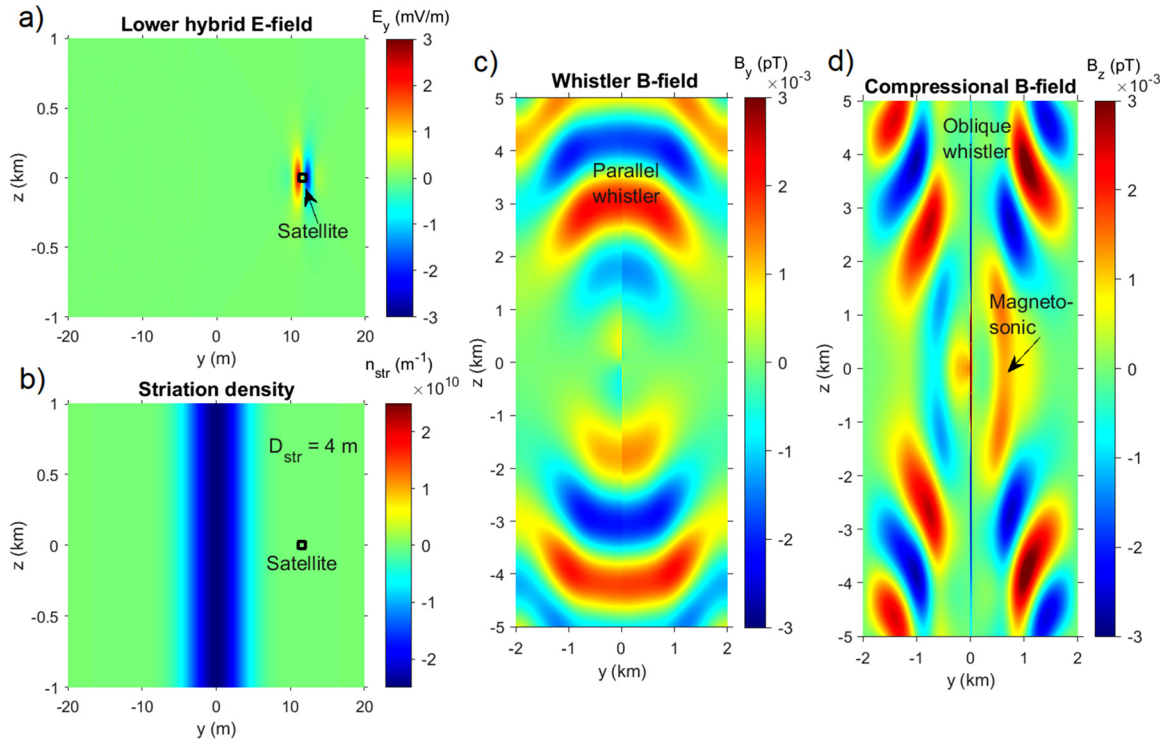

FIG. 7. Simulation of a satellite of size $D_{sat} = 1$ m crossing a striation of width $D_{str} = 4$ m at at time $t = 0$. At $t = 1.5$ ms, the satellite [panel (a)] has interacted with the striation [panel (b)] to generate a long wavelength modulated pulse of parallel and oblique whistler waves [panels (c) and (d)] as well as a magnetosonic wave [panel (d)]. Only a local field near the satellite [panel (a)] is generated, but no train of lower hybrid waves behind the satellite.

$$t - t_0 = \frac{L}{v_g} = \frac{L}{2\lambda_e \omega_{ce}} \sqrt{\frac{\omega_{ce}}{\omega}}, \tag{29}$$

is shorter for higher frequencies than lower frequencies, giving the characteristic descending whistler tone. Solving for frequency gives

$$\omega(t) = \frac{1}{4\omega_{ce}(t - t_0)^2} \frac{L^2}{\lambda_e^2}. \tag{30}$$

Because the time t_0 is, in general, unknown or hard to estimate, it is convenient to relate $\omega(t)$ to its time derivative, which both can be estimated from the spectrogram. The time-derivative of the frequency is

$$\dot{\omega}(t) \equiv \frac{d\omega}{dt} = -\frac{1}{2\omega_{ce}(t - t_0)^3} \frac{L^2}{\lambda_e^2} = -\frac{4\lambda_e \omega_{ce}^2}{L} \left(\frac{\omega}{\omega_{ce}}\right)^{3/2}, \tag{31}$$

where Eq. (29) was used to eliminate $t - t_0$. Finally, solving for distance gives

$$L = 4\lambda_e \frac{\omega_{ce}^2}{(-\dot{\omega}(t))} \left(\frac{\omega(t)}{\omega_{ce}}\right)^{3/2}. \tag{32}$$

Hence, measuring the frequency $\omega(t)$ and frequency drift $\dot{\omega}(t)$ at a certain time, the distance L to the space debris can be estimated. In Fig. 11, we study the signal at frequency $f = 4$ kHz corresponding to $\omega = 2\pi f = 2.5 \times 10^4\ \mathrm{s}^{-1}$. The estimated frequency drift at that frequency (green dashed–dotted line) is $\dot{f} \approx -10$ kHz/ms corresponding to $\dot{\omega} \approx -6.3 \times 10^7 \mathrm{s}^{-1}/\mathrm{s}$. Using that $\lambda_e = 7.52$ m and $\omega_{ce} = 8.44 \times 10^6\ \mathrm{s}^{-1}$ (cf. Table I), Eq. (32) gives the estimated distance $L = 5.5$ km, near the true distance 5 km.

On the other hand, in the direction perpendicular to the magnetic field, the generated wave can propagate as a dispersive magnetosonic (MS) wave, which has the lower hybrid frequency as the electrostatic resonance. Figure 12 shows the same simulation as in Fig. 11, but the signal is recorded 1 km away from the satellite perpendicular to the magnetic field at $y = 1$ km, $z = 0$. Here, the signal is weaker, but one can identify the magnetosonic wave which has a rising tone with time.

The dispersion relation (8) for perpendicularly propagating dispersive magnetosonic waves gives the frequency $\omega = \lambda_e k_\perp \omega_{\mathrm{LH}} / \sqrt{1 + \lambda_e^2 k_\perp^2}$, and the corresponding wavenumber $k_\perp = \lambda_e^{-1}(\omega/\omega_{\mathrm{LH}}) / \sqrt{1 - \omega^2/\omega_{LH}^2}$, with a resonance at $\omega = \omega_{\mathrm{LH}}$. The time for a wave created at $t = t_0$ to propagate a distance L is $t - t_0 = L/v_{\mathrm{g}}$ where the group velocity is

$$v_{\mathrm{g}} = \frac{\partial \omega}{\partial k_\parallel} = \frac{\lambda_e \omega_{\mathrm{LH}}}{\left(1 + \lambda_e^2 k_\perp^2\right)^{3/2}} = v_{\mathrm{A}} \left(1 - \omega^2/\omega_{\mathrm{LH}}^2\right)^{3/2}, \tag{33}$$

with $v_{\mathrm{A}} = \lambda_e \omega_{\mathrm{LH}}$ being the Alfvén speed. In contrast to the whistler waves, the group velocity for the dispersive magnetosonic wave is highest, $v_{\mathrm{g}} = v_{\mathrm{A}}$, for low frequencies $\omega \to 0$, and decreases to zero at the electrostatic lower hybrid resonance $\omega \to \omega_{\mathrm{LH}}$. Hence, the time taken to propagate a distance L,

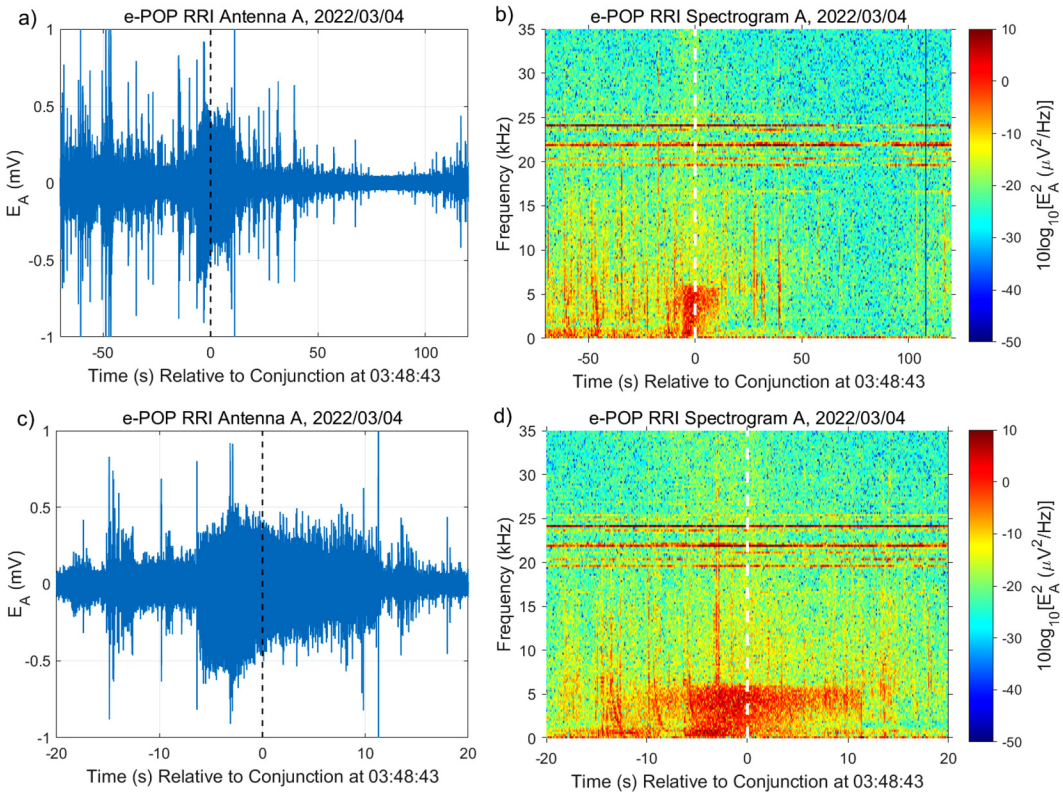

FIG. 8. (a) Wave amplitude and (b) power spectrogram [close-ups in time in (c) and (d)] measured by Swarm-E/e-POP during conjunction with Starlink 2521 on 2022/03/04 at 03:48:43, where a FLASH event was observed associated with a burst of waves with spectral components above the ion cyclotron frequency up to the lower hybrid frequency. Vertical dashed lines indicate the time of conjunction. In (a) and (c) a low-pass filter is applied to show only waves below 15 kHz. Strong emissions at 18–25 kHz in (b) and (d) are due to VLF radio stations. Short excitations above 7 kHz are due to lightning-excited whistlers from thunderstorms. A vertical dark blue stripe in (b) at $t = 110$ s is due to missing data.

$$t - t_0 = \frac{L}{v_g} = \frac{L}{v_A\left(1 - \omega^2/\omega_{LH}^2\right)^{3/2}}, \tag{34}$$

is shorter for lower frequencies. Solving for $\omega(t)$ gives

$$\omega(t) = \omega_{LH}\sqrt{1 - \left((t - t_0)v_A/L\right)^{-2/3}}. \tag{35}$$

Note that the signal with frequency $\omega(t)$ is "switched on" and exists only for $t - t_0 > L/v_A$, after which the frequency increases with time. Also here, because the time t_0 is unknown, it is more convenient to relate $\omega(t)$ to its time derivative

$$\dot{\omega}(t) \equiv \frac{d\omega}{dt} = \frac{\omega_{LH}\left(L/v_A\right)^{2/3}(t - t_0)^{-5/3}}{3\left(1 - \left((t - t_0)v_A/L\right)^{-2/3}\right)^{1/2}}$$
$$= \frac{\omega_{LH}v_A}{3L}\frac{\omega_{LH}}{\omega}\left(1 - \frac{\omega^2}{\omega_{LH}^2}\right)^{5/2}, \tag{36}$$

where Eq. (32) was used to eliminate $t - t_0$. Solving for the distance gives

$$L = \frac{\omega_{LH}v_A}{3\dot{\omega}(t)}\frac{\omega_{LH}}{\omega(t)}\left(1 - \frac{\omega^2(t)}{\omega_{LH}^2}\right)^{5/2}. \tag{37}$$

Using frequency $\omega(t)$ and frequency drift $\dot{\omega}(t)$ at a certain time, the distance L to the space debris can be estimated. In Fig. 12, we study the signal having the frequency $f = 3$ kHz corresponding to $\omega = 2\pi f = 1.9 \times 10^4\ \mathrm{s}^{-1}$, where the estimated frequency drift (green line) is $\dot{f} \approx 1.36$ kHz/ms corresponding to $\dot{\omega} \approx 8.6 \times 10^6 \mathrm{s}^{-1}/\mathrm{s}$, which from Eq. (37), with $v_A = 372$ km/s and $\omega_{LH} = 2\pi \times 7.87$ kHz $= 49.4 \times 10^3\ \mathrm{s}^{-1}$ (cf. Table I), gives the estimated distance $L = 1.2$ km, comparable to the true distance 1 km.

To uniquely determine the position of the space debris or satellite, one needs both the distance L calculated above and the direction to the satellite. A possible way to obtain the direction is via the Poynting flux

$$\mathbf{S} = \frac{\mathbf{E} \times \mathbf{B}}{\mu_0} \tag{38}$$

of the generated electromagnetic whistler and magnetosonic waves. Since the wave carries energy away from the space debris, the Poynting flux is expected to be directed away from the space debris, while its negative points in the direction toward the space debris. The Poynting flux fluctuates in time with the wave, but of interest for direction finding is the average Poynting flux. By defining the unit vector

$$\hat{\mathbf{L}} = -\frac{\langle \mathbf{S} \rangle}{|\langle \mathbf{S} \rangle|}, \tag{39}$$

where the angular brackets denote averaging over time, then the vector

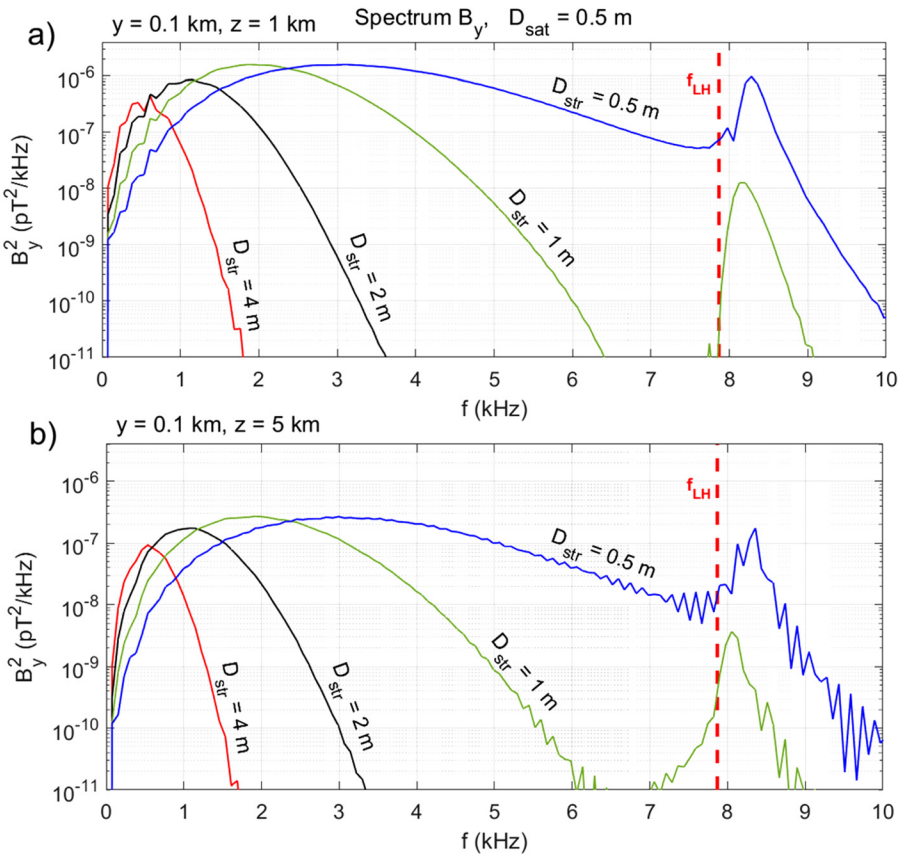

FIG. 9. Frequency spectra of generated whistler wave magnetic field B_y at (a) $z = 1$ km and (b) $z = 5$ km away from the satellite along the magnetic field lines for striation widths $D_{str} = 0.5$ m (blue), $D_{str} = 1$ m (green), $D_{str} = 2$ m (black), and $D_{str} = 4$ m (red), for a satellite of size $D_{sat} = 0.5$ m. The vertical dashed red line indicates the lower hybrid frequency $f_{LH} = 7.87$ kHz.

$$\mathbf{L} = \hat{\mathbf{L}}L \tag{40}$$

describes the estimated spatial vector from the observer to the space debris.

Figures 13 and 14 show the wave electric and magnetic wave fields at time $t = 0.7$ ms after a satellite of size $D_{sat} = 0.5$ m has crossed a striation of size $D_{str} = 0.5$ m, with whistler waves propagating away from $(y, z) \approx (0, 0)$ within a cone to the magnetic field. The resulting Poynting flux is shown in Fig. 15. The y-component of the Poynting flux [Fig. 15(b)] is mostly positive for positive y and negative for negative y, while the z-component [Fig. 15(c)] is positive for positive z and negative for negative z. Hence, the Poynting flux is directed away from $(y, z) \approx (0, 0)$ where the whistler wave was excited by the satellite crossing the striation. The x-component in panel (a) is oscillatory and on average very small in the y–z plane.

In Fig. 16, the Poynting flux averaged in time over 0.32 ms is used to calculate the direction unit vector $\hat{\mathbf{L}}$ in Eq. (37), shown as arrows in Figs. 16(b) and 16(c). It is seen that $\hat{\mathbf{L}}$, in general, points toward the location $(y, z) = (0, 0)$ where the whistler waves were excited by the satellite-striation interaction. One arrow, at $y = -1$ km, $z = 0$, where the Poynting flux is very weak, points in the "wrong" direction away from the satellite. At later times beyond a few millisecond, the measurements outside the whistler resonance cone (19.5° to $\mathbf{B}_0$) lose accuracy, while within the whistler cone the arrows point in the direction toward the satellite.

While the wave energy for the whistler wave is almost exclusively in the wave magnetic field, the dispersive magnetosonic waves will have much of its energy in the kinetic energy $m_e v_e^2/2$ of electrons performing $\mathbf{E} \times \mathbf{B}$ drift in the wave electric field and in the kinetic energy $m_i v_i^2/2$ of the ion oscillations. Therefore, the Poynting flux may contain only a minor part of the energy flux for the dispersive magnetosonic waves, which makes the measurement of energy flux and its interpretation more challenging for the magnetosonic waves compared to the whistler waves.

VI. CONCLUSIONS

The present work has investigated wave generation by electrically charged satellites or space debris propagating through the ionosphere at an angle to the magnetic field in the presence of magnetic field aligned irregularities (striations). The satellite constitutes a local current density pulse propagating at the velocity $\mathbf{v}_{sat}$ (typically 7.7 km/s at an altitude 300 km) relative to the background plasma. This creates local time-dependent magnetic and electric fields that interact with the plasma particles to generate waves. In a homogeneous plasma, satellites of sizes $D_{sat} < 0.5$ m can efficiently excite lower hybrid waves in a wake behind the satellite, with a wavelength $\lambda_{LH} = v_{sat}/f_{LH} \approx 1$ m for a lower hybrid frequency $f_{LH} \approx 7.87$ kHz. The lower hybrid waves spread along the magnetic field line with a speed $|v_\parallel| < v_{sat}\sqrt{m_i/8m_e} = 465$ km/s and form a wedge behind the satellite.

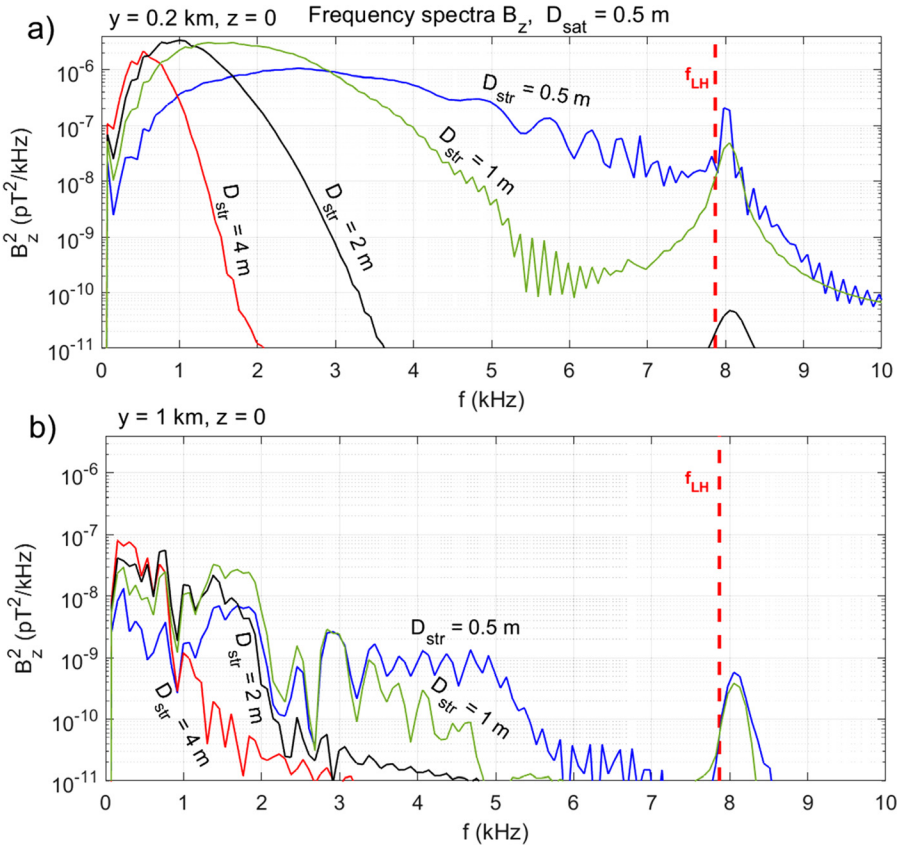

FIG. 10. Frequency spectra of generated compressional magnetic field B_z at (a) $z = 0.2$ km and (b) $z = 1$ km away from the satellite across the magnetic field lines, for striation widths $D_{str} = 0.5$ m (blue), $D_{str} = 1$ m (green), $D_{str} = 2$ m (black), and $D_{str} = 4$ m (red), for a satellite of width $D_{sat} = 0.5$ m. The vertical dashed red line indicates the lower hybrid frequency $f_{LH} = 7.87$ kHz.

For larger satellites $D_{sat} > 1$ m, the generation of lower hybrid waves by the satellite becomes less efficient.

Magnetic field aligned striations are crucial for the generation of whistler and compressional Alfvén waves by the satellite, either via direct interaction with the satellite or via mode conversion of the satellite-generated lower hybrid waves to whistler waves. Striations are efficiently produced during ionospheric heating experiments, and have been observed by rockets at Arecibo (Kelley *et al.*, 1995; Bernhardt *et al.*, 1995a; 1995b) with typical length scales perpendicular to the magnetic field ranging from below a meter up to kilometers, with a peak at around 10 m. Supersmall scale striations of size 0.1 m may also be generated (Najmi *et al.*, 2014; 2015) when the HF frequency is tuned slightly above electron cyclotron harmonics. The striations may extend several tens of kilometers parallel to the background magnetic field [e.g., Kelley *et al.* (1995)], and hence, groups of striations generated during ionospheric heating experiments can have significant cross sections to interact with low earth orbit (LEO) satellites or space debris overflying the heating facility. Striations are also created naturally at higher altitudes via various plasma processes and instabilities.

The most efficient generation of whistler waves occurs for supersmall-scale striations of size $D_{str} \approx 0.25$ m and small satellites, through the mode conversion of satellite-generated lower hybrid waves. The whistler waves propagate away from the satellite within a cone 19.5° to the background magnetic field and with a frequency near or slightly above the lower hybrid frequency. For larger striations, $D_{str} > 1$ m, the mode conversion of lower hybrid to whistler waves becomes inefficient, and the main generation mechanism of whistler waves is the direct interaction between the satellite and the striation leading to short, modulated pulses propagating away from the satellite. Larger striations and satellites produce whistler waves with longer wavelengths and correspondingly lower frequencies, of up to a few kHz. In addition, modulated pulses of dispersive magnetosonic waves are also generated which propagate at large angles to the magnetic field.

The results are consistent with the observed FLASH events during satellite conjunctions (Bernhardt *et al.*, 2023), in which a burst of waves with frequencies ranging from the ion cyclotron frequency to the lower hybrid frequency were observed. In addition to frequency spectra, future experiments should determine the direction and distance to the space debris as discussed in Sec. V E and summarized in Table IV. If the spacecraft is equipped with a low frequency vector sensor that simultaneously measures the electric and magnetic wave fields, then the direction to the satellite or space debris can be determined via the average Poynting flux of the satellite-generated waves. On the other hand, by using the dispersive properties of the wave and studying the wave frequency and the change of frequency with time using a plasma wave receiver, the distance to the space debris can be estimated, which complements the direction finding to determine the location of the space debris.

In this first work, we have used a linear model to study how waves can be excited by a charged object propagating through plasma. A linear wave propagation model is reasonable, since the waves

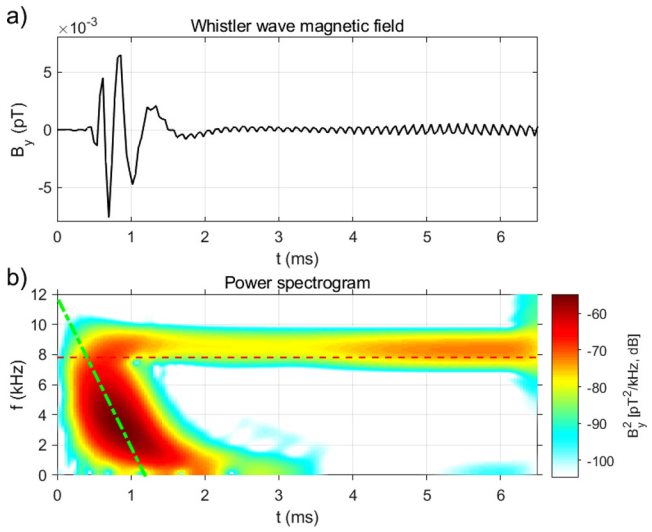

FIG. 11. (a) The whistler wave magnetic field generated detected 5 km away along the magnetic field from a satellite crossing the striation at $t = 0$ and (b) the corresponding spectrogram using a sin-squared time window of width 1.2 ms. The large amplitude pulse of amplitude $\approx 7 \times 10^{-3}$ pT in panel (a) has a descending frequency which decreases about 10 kHz/ms at $f = 4$ kHz, indicated by a dashed-dotted green line in panel (b). The mode conversion of LH waves to whistlers gives rise to the sustained signal of amplitude $\approx 5 \times 10^{-4}$ pT in panel (a), slightly above the LH frequency indicated by a dashed red line in panel (b).

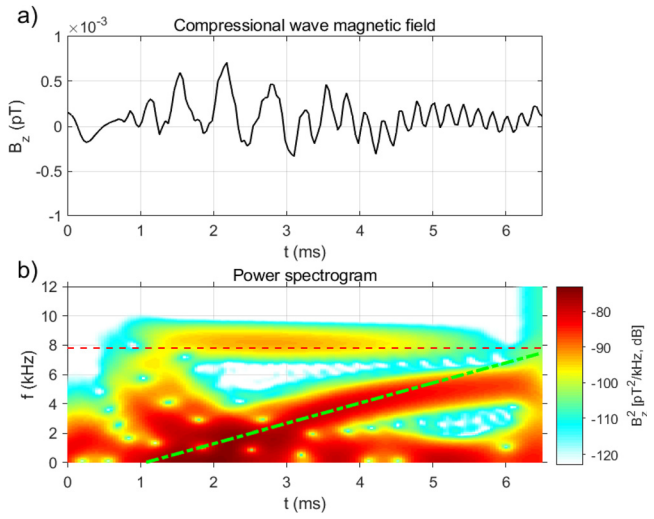

FIG. 12. (a) The compressional wave magnetic field generated detected 1 km away perpendicular to the magnetic field from a satellite crossing the striation at $t = 0$, and (b) the corresponding spectrogram using a sin-squared time window of width 1.2 ms. The dispersive magnetosonic pulse in panel (a) has an ascending frequency which increases by about 1.35 kHz/ms, indicated by a dashed-dotted green line in panel (b). The mode conversion of LH waves to whistlers gives rise to the weak signal slightly above the LH frequency, indicated by a dashed red line in panel (b).

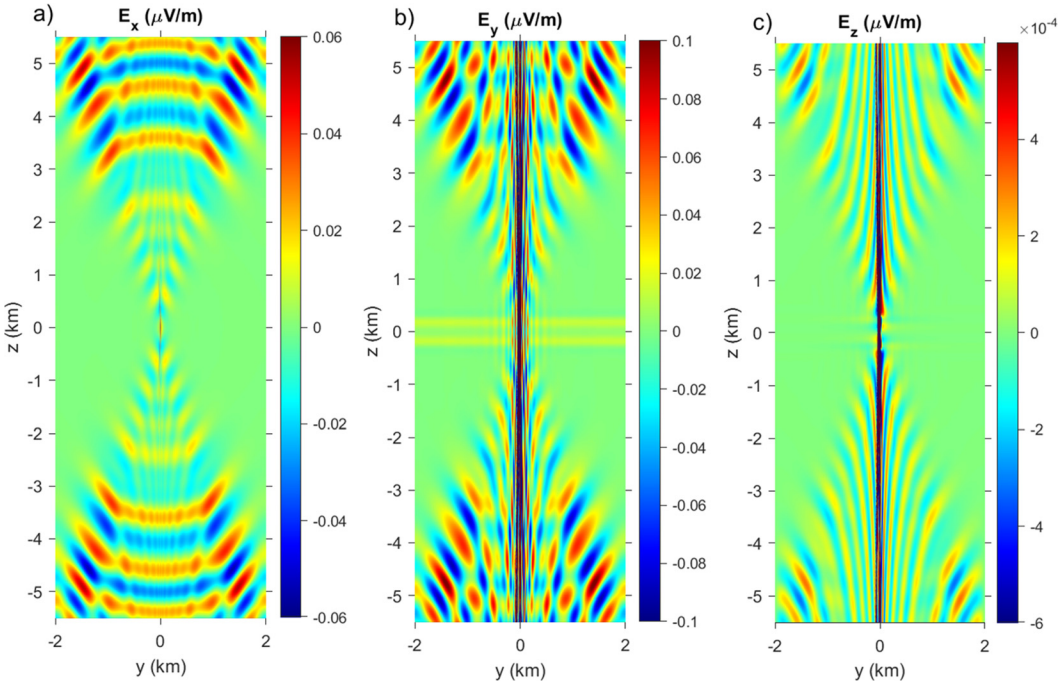

FIG. 13. The x, y, and z components of the wave electric field at $t = 0.7$ ms.

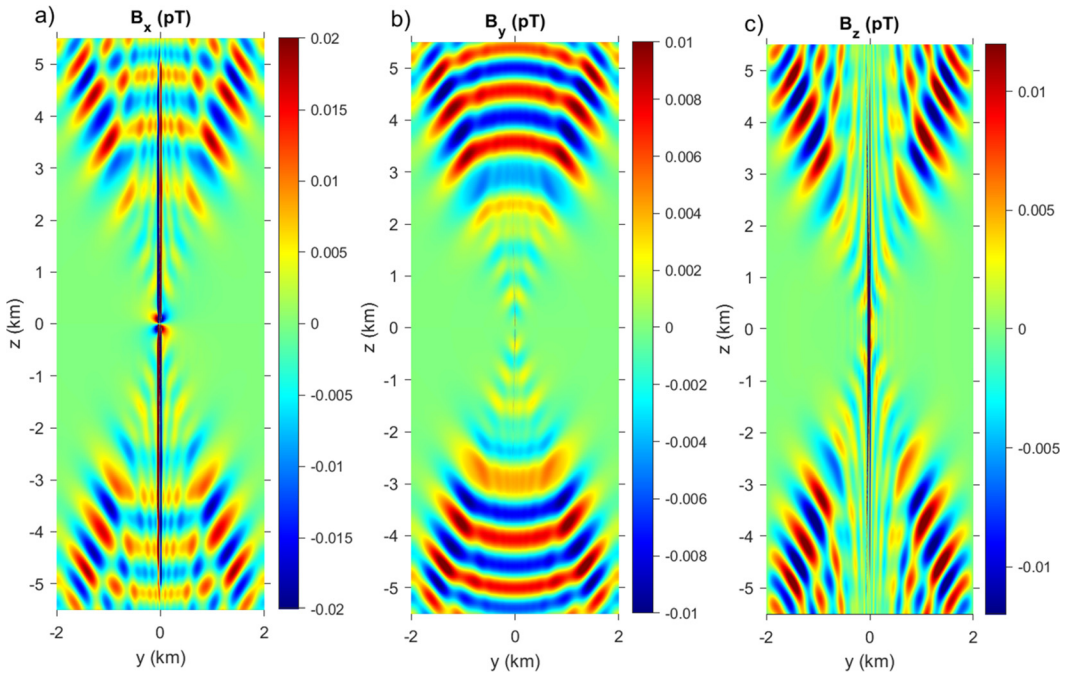

FIG. 14. The x, y, and z components of the wave magnetic field at $t = 0.7$ ms.

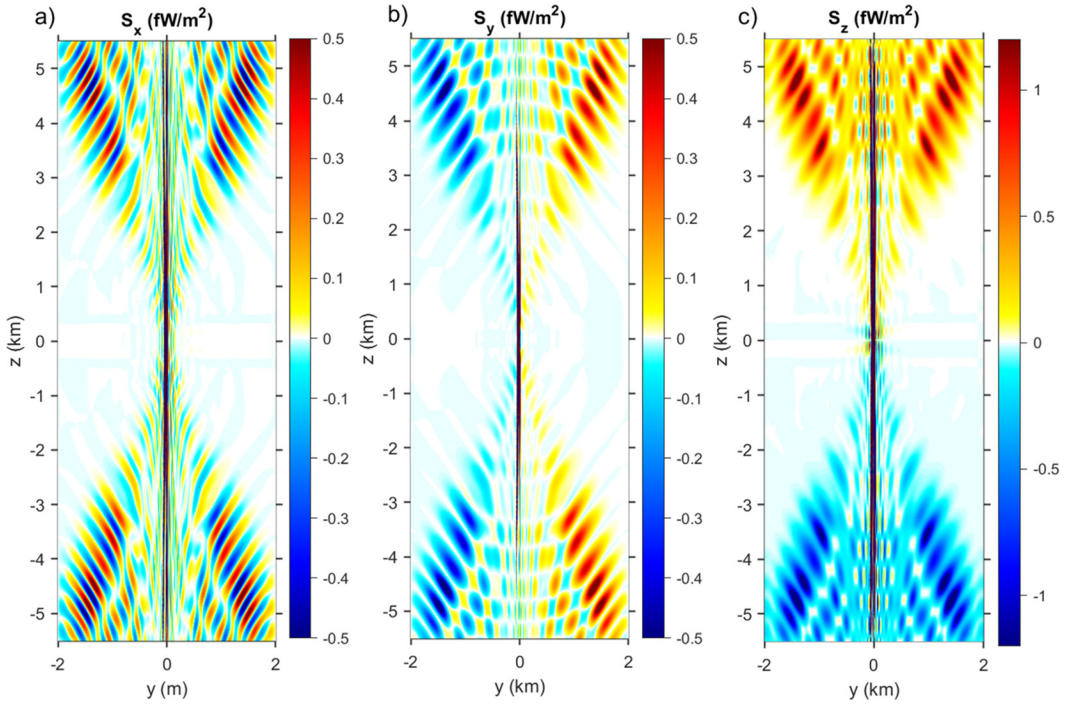

FIG. 15. Panels (a)–(c): The x, y, and z components of the Poynting flux $\mathbf{S} = \mathbf{E} \times \mathbf{B}/\mu_0$ (in femtowatt per meter, fW/m) at $t = 0.7$ ms.

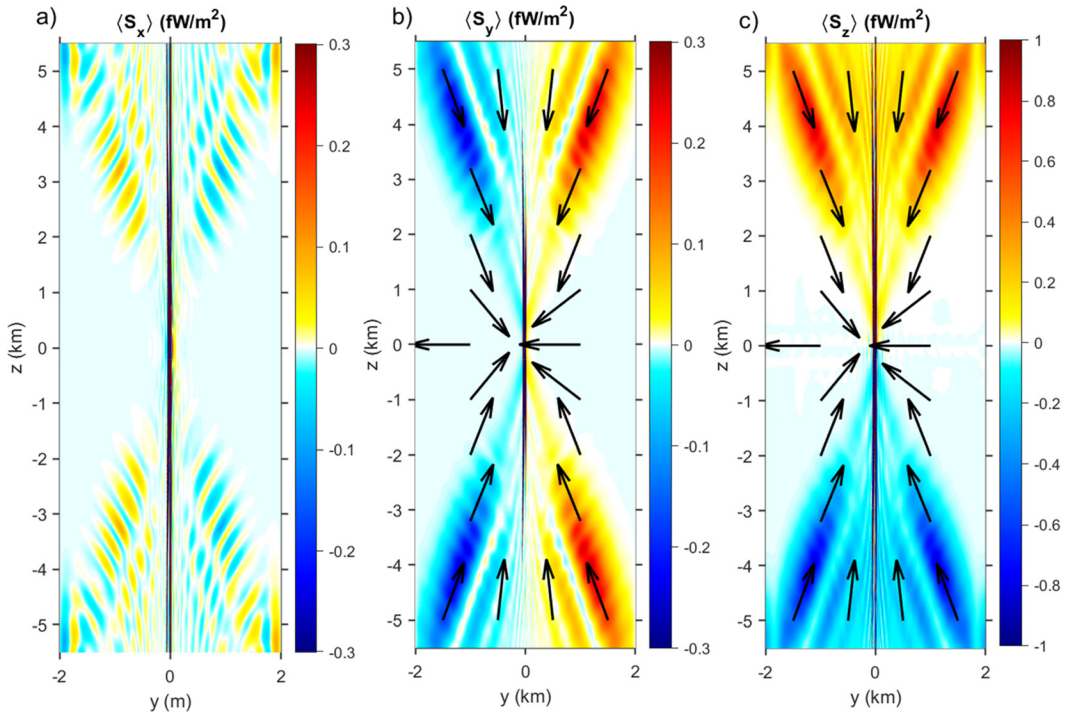

FIG. 16. Panels (a)–(c): The x, y, and z components of the Poynting flux (cf. Fig. 15) averaged over 0.32 ms. The arrows in panels (b) and (c) show the unit vector $\hat{L}$ [cf. Eq. (37)] calculated from the averaged Poynting flux at the base of each arrow at different spatial locations. The averaged $\langle S_x \rangle$ component [panel (a)] is small compared to S_y and S_z.

generated by the satellites have low amplitudes ($B < 1\,\mathrm{pT}$ and $E \sim 10\,\mathrm{mV/m}$). Closest to the satellite surface, however, the interaction between the satellite and background plasma is probably nonlinear, including the interaction with striations. Furthermore, in the presence of large amplitude lower hybrid waves generated by rocket exhaust or other processes, there are observations of amplification of whistler waves via parametric amplification [e.g., Bernhardt *et al.* (2022)]. Future work will include nonlinear terms in the wave model and the interaction near the satellite. Also, the present nonlinear satellite charging model will be improved by including different scenarios of streaming ions and precipitating electrons, and by considering the impact of the ambient magnetic field on charging.

Comparing with the e-POP RRI observations in Fig. 8, it was, however, noted that the simulated signals are too weak to account for the strong emissions in the FLASH event during conjunction. The satellite-generated lower hybrid waves, on the other hand, can have amplitudes of several millivolt per meter, as seen in Fig. 4 and Table II, and would give very strong signals. However, in homogeneous plasma, these lower hybrid waves only propagate in a very narrow cone to the magnetic field and behind the satellite and may, therefore, be difficult to detect by a neighboring spacecraft unless the wave energy can spread in space by some mechanism. One potential mechanism could be that lower hybrid waves are generated by the satellite within larger density cavities where the local lower hybrid frequency is lower due to the relation [e.g., Swanson (2003)] $\omega_{\mathrm{LH}}^2 = \omega_{ce}\omega_{ci}/(1 + \omega_{ce}^2/\omega_{pe}^2)$, and that these lower hybrid waves leak magnetosonic waves (Hall, 2004; Hall *et al.*, 2004) when they reach the boundaries of the cavities. This will also be investigated in future research.

ACKNOWLEDGMENTS

This research was based upon the work supported in part by the Office of the Director of National Intelligence (ODNI), Intelligence Advanced Research Projects Activity (IARPA), via 2023-23060200005. The views and conclusions contained herein are those of the authors and should not be interpreted as necessarily representing the official policies, either expressed or implied, of ODNI, IARPA, or the U.S. Government. The U.S. Government is authorized to reproduce and distribute reprints for governmental purposes notwithstanding any copyright annotation therein. The work was carried out in collaboration with Blue Halo on the IARPA SINTRA program. Simulation results were obtained using the ARCHIE-WeSt High-Performance Computer (www.archie-west.ac.uk) based at the University of Strathclyde. B.E. acknowledges the EPSRC (UK) (Grant Nos. EP/R004773/1 and EP/M009386/1). All simulation data are contained in the figures. CASSIOPE/Swarm-E e-POP data can be accessed via University of Calgary, https://epop.phys.ucalgary.ca/data/. Discussions with Andrew Howarth at University of Calgary are gratefully acknowledged.

AUTHOR DECLARATIONS

Conflict of Interest

The authors have no conflicts to disclose.

Author Contributions

Bengt Eliasson: Formal analysis (equal); Software (equal); Writing – original draft (equal); Writing – review & editing (equal). **Paul A.**

Bernhardt: Conceptualization (equal); Funding acquisition (equal); Project administration (equal); Writing – review & editing (equal).

DATA AVAILABILITY

The data that support the findings of this study are available from the corresponding author upon reasonable request.

APPENDIX A: ION LANDAU DAMPING OF SATELLITE-GENERATED ION-ACOUSTIC WAVES

We here discuss how ion Landau damping may attenuate ion-acoustic waves triggered by hypersonic space objects. A number of authors have discussed ion-acoustic pinned and precursor solitons with applications of detecting space debris, and we mention a few:

Kumar and Sen (2020) used particle-in-cell (PIC) simulations of magnetosonic and ion-acoustic precursor solitons. For ion-acoustic solitons, they used the reduced ion-to-electron mass ratio $m_i/m_e = 25$, the ion temperatures $T_i = 0.1$ eV, and a relativistically high electron temperature $T_e = 125$ keV (hence $T_e/T_i \sim 10^6$) such that the ion-acoustic speed is very high, $C_s = \sqrt{k_B T_e/m_i} = 0.1c$ with c being the speed of light, which reduces ion Landau damping significantly allowing ion-acoustic precursor solitons to exist for long time. The very high electron temperature (about 100 times hotter than the Sun's interior!) is, however, not representative for ionospheric plasmas.

Sen *et al.* (2015), Tiwari and Sen (2016), and Truitt and Hartzell (2020a) used simulations of the forced Korteweg–de Vries (K-dV) equation with cold ions and hence neglected Landau damping in their models. However, since the electron and ion temperatures are comparable in the ionosphere, ion Landau damping becomes important and cannot be neglected.

We find the paper by Truitt and Hartzell (2020b) most interesting, where they used a forced K-dV equation with an ion Landau damping rate motivated by kinetic theory. They discuss centimeter-sized precursor and pinned ion-acoustic solitons with propagation distances of several kilometers, and where pre-cursor solitons could exist in the upper LEO with hydrogen-rich plasma. We believe that, however, the longevity of the ion-acoustic solitons has been over-estimated by under-estimating the Landau damping rate by using an approximate formula by Arshad *et al.* (2011) for ion-acoustic Landau damping in multi-ion plasma.

The ion-acoustic Landau damping rate γ used by Truitt and Hartzell (2020b) for kappa-distributed two-ion plasmas (Arshad *et al.*, 2011) is written as

$$\frac{\gamma_\kappa}{\omega_r} = -\sqrt{\frac{\pi}{8}}\frac{\Gamma(\kappa+1)}{\Gamma(\kappa-1/2)}\frac{\sqrt{N_0^{12}}}{2^{3/2}(\kappa-1/2)^{3/2}} \times \left[\sqrt{\frac{m_e}{m_{i1}}} + \frac{n_{0i1}}{n_{0e}}\beta^{3/2}\left[1+\frac{\beta N_0^{12}}{2(2\kappa-1)}+\frac{3\delta}{(2\kappa-3)N_0^{12}}\right]^{-\kappa-1} + \frac{n_{0i2}}{n_{0e}}\beta^{3/2}\sqrt{\frac{m_{i2}}{m_{i1}}}\left[1+\frac{\beta N_0^{12}}{2(2\kappa-1)}+\frac{3\delta}{(2\kappa-3)N_0^{12}}\frac{m_{i2}}{m_{i1}}\right]^{-\kappa-1}\right], \quad \text{(A1)}$$

where ω_r is the angular frequency of the ion-acoustic wave, $\beta = T_e/T_i$, $N_0^{12} = n_{0i1}/n_{0e} + (n_{0i2}/n_{0e})(m_{i1}/m_{i2})$, and $\delta = n_{0i1}/n_{0e} + (n_{0i2}/n_{0e})(m_{i1}/m_{i2})^2$ are relationships between the dominant ion density n_{0i1}, secondary ion density n_{0i2}, electron density n_{0e}, dominant ion mass m_{i1}, and secondary ion mass m_{i2}, and quasi-neutrality requires that $n_{0e} = n_{0i1} + n_{0i2}$. In the numerical evaluation, $\kappa = 100$ was used for the kappa-distributed ions. It was assumed in low LEO that ion species 1 is O+ and ion species 2 is H+. The numerical evaluation of the damping rate as a function of electron-to-ion temperature ratio β shows an increasing damping rate $|\gamma/\omega_r|$ with increasing β [cf. Figs. 1 and 2 of Truitt and Hartzell (2020b)], but from kinetic theory one would expect the ion-acoustic Landau damping to decrease with increasing β.

To compare with exact theory we focus on the case of one ion species O+, with $n_{i02} = 0$, where one has $n_{i01}/n_{e0} = 1$, $N_0^{12} = 1$, and $\delta = 1$, and the damping rate (A1) takes the following form:

$$\frac{\gamma_\kappa}{\omega_r} = -\sqrt{\frac{\pi}{8}}\frac{\Gamma(\kappa+1)}{\Gamma(\kappa-1/2)}\frac{1}{2^{3/2}(\kappa-1/2)^{3/2}} \times \left[\sqrt{\frac{m_e}{m_{i1}}} + \beta^{3/2}\left[1+\frac{\beta}{2(2\kappa-1)}+\frac{3}{(2\kappa-3)}\right]^{-\kappa-1}\right]. \quad \text{(A2)}$$

This damping rate, with $\kappa = 100$, is plotted as a solid blue line in Fig. 17 and agrees with Fig. 1 of Truitt and Hartzell (2020b). In the "Maxwellian limit" $\kappa \to \infty$, the formula (A2) converges to

$$\frac{\gamma_{\kappa\to\infty}}{\omega_r} = -\sqrt{\frac{\pi}{8}}2^{-3/2}\left[\sqrt{\frac{m_e}{m_{i1}}} + \beta^{3/2}\exp\left(-\frac{\beta}{4}-\frac{3}{2}\right)\right], \quad \text{(A3)}$$

plotted as a dashed blue line in Fig. 17, and which almost coincides with the solid blue line. The commonly used approximate formula for Maxwell distributed plasma [e.g., Chen (1984)]

$$\frac{\gamma_M}{\omega_r} = -\sqrt{\frac{\pi}{8}}\left[\sqrt{\frac{m_e}{m_{i1}}} + \beta^{3/2}\exp\left(-\frac{\beta}{2}-\frac{3}{2}\right)\right] \quad \text{(A4)}$$

is plotted as a dashed black line in Fig. 17. It has the same general form as Eq. (A3) but with some differences in numerical factors in front of the square brackets and inside the exponentials, making the damping rate Eq. (A3) smaller for $\beta < 4$ and significantly larger for $\beta > 5$. A numerical solution of the exact kinetic dispersion relation for Maxwell-distributed electrons and ions (given below) is plotted as a red dashed–dotted line in Fig. 17 and is consistent with for example the numerical solution by Chen (1984) in his Figs. 7–31. It is seen that the exact γ/ω_r becomes large for small β, in contrast to the formula by Arshad *et al.* (2011) which predicts decreasing γ/ω_r with decreasing β for $\beta < 6$. For typical values of $\beta \sim 1.1 - 1.5$ [see Fig. 9 of Truitt and Hartzell (2020a; 2020b)], the exact kinetic dispersion relation gives $\gamma/\omega_r \sim 0.3 - 0.4$ while the approximate formula by Arshad *et al.* (2011) gives almost an order of magnitude smaller damping $\gamma/\omega_r \sim 0.05$. Exact kinetic treatment predicts that ion-acoustic waves in the ionosphere are highly attenuated by ion Landau damping and will not propagate far from the space debris that launched them, while the approximate formulas strongly underestimate the damping.

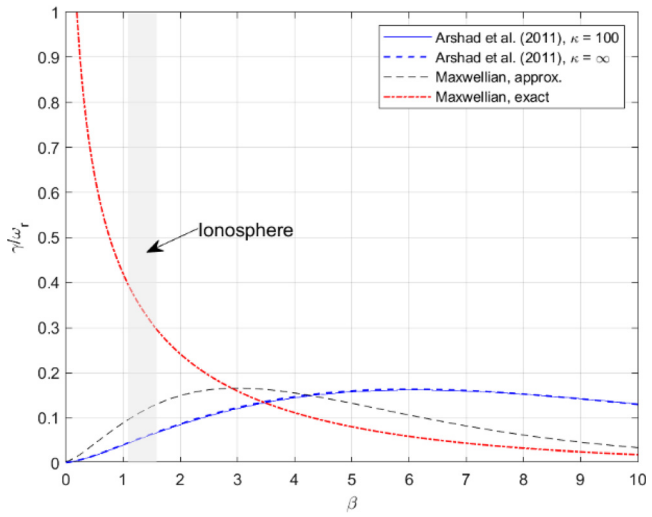

FIG. 17. Landau damping rates: For kappa-distributed plasma (Arshad *et al.*, 2011) for $\kappa = 100$ (blue solid line) and $\kappa = \infty$ (blue dashed line); for Maxwell-distributed plasma (Chen, 1984), black dashed line); and exact dispersion relation for Maxwell-distributed plasma (red curve). The shaded region indicates typical ionospheric conditions with $\beta = T_e/T_i \sim 1.1 - 1.5$ (Truitt and Hartzell, 2020b).

The main cause of underestimation of ion Landau damping is that the approximate formulas involve asymptotic expansions of the kinetic ion susceptibilities under the assumption $\beta \gg 1$, which breaks down for ionospheric conditions with $\beta \sim 1$, as seen in Fig. 17. A discussion about the accuracy of different models of Landau damping in un-magnetized plasma is given by McKinstrie *et al.* (1999).

For reference, the dispersion relation for ion-acoustic waves in un-magnetized electron–ion plasma reads

$$1 + \chi_i + \chi_e = 0, \tag{A5}$$

where the respective susceptibilities for Maxwell distributed ions and electrons are

$$\chi_i = \frac{\omega_{pi}^2}{v_{Ti}^2 k_{IA}^2}\left(1 + \xi_i Z(\xi_i)\right) \tag{A6}$$

and

$$\chi_e = \frac{\omega_{pe}^2}{v_{Te}^2 k_{IA}^2}\left(1 + \xi_e Z(\xi_e)\right). \tag{A7}$$

Here, the plasma dispersion function (Fried and Conte, 1961; Huba, 1994) can be written as follows:

$$Z(\xi) = e^{-\xi^2}\left(i\sqrt{\pi} - 2\int_0^{\xi} e^{t^2} dt\right) \tag{A8}$$

with $\xi_i = \omega_{IA}/\left(\sqrt{2}v_{Ti}k_{IA}\right)$ and $\xi_e = \omega_{IA}/\left(\sqrt{2}v_{Te}k_{IA}\right)$, and where $v_{Ti} = \sqrt{k_B T_i/m_i}$ and $v_{Te} = \sqrt{k_B T_e/m_e}$ are the ion and electron thermal speeds, and $\omega_{pi} = \sqrt{n_0 e^2/\epsilon_0 m_i}$ and $\omega_{pe} = \sqrt{n_0 e^2/\epsilon_0 m_e}$ are the ion and electron angular plasma frequencies, respectively. The ion-acoustic wavenumber k_{IA} is assumed to be real, while the wave frequency is assumed complex valued, $\omega_{IA} = \omega_r - i\gamma$. In the long wavelength limit, the dispersion relation simplifies to $\chi_i + \chi_e = 0$ and the damping rate γ/ω_r depends only on $\beta = T_e/T_i$ but not on k_{IA}.

APPENDIX B: DERIVATION OF THE WAVE EQ. (5)

To convert the system (1)–(4) to Eq. (5) amenable for numerical simulations, we first solve for **E** in Eq. (2) and insert the result in Eqs. (1) and (3),

$$m_i \frac{\partial \mathbf{v}_i}{\partial t} = -e\left(\mathbf{v}_e \times \mathbf{B}_0 + \frac{m_e}{e}\frac{\partial \mathbf{v}_e}{\partial t}\right), \tag{B1}$$

$$\frac{\partial \mathbf{B}}{\partial t} = \nabla \times \left(\mathbf{v}_e \times \mathbf{B}_0 + \frac{m_e}{e}\frac{\partial \mathbf{v}_e}{\partial t}\right). \tag{B2}$$

For convenience we define the particle number current densities $\mathbf{j}_i = \tilde{n}(\mathbf{r}_\perp)\mathbf{v}_i$ and $\mathbf{j}_e = \tilde{n}(\mathbf{r}_\perp)\mathbf{v}_e$ in Eqs. (4), (B1), and (B2), with the result

$$\nabla \times \mathbf{B} = \mu_0 e(\mathbf{j}_i - \mathbf{j}_e) + \mu_0 \mathbf{v}_{\rm sat}\,\rho_{\rm sat}(\boldsymbol{\xi}), \tag{B3}$$

$$m_i \frac{\partial \mathbf{j}_i}{\partial t} = -e\left(\mathbf{j}_e \times \mathbf{B}_0 + \frac{m_e}{e}\frac{\partial \mathbf{j}_e}{\partial t}\right), \tag{B4}$$

$$\frac{\partial \mathbf{B}}{\partial t} = \nabla \times \left(\frac{1}{\tilde{n}(\mathbf{r}_\perp)}\left(\mathbf{j}_e \times \mathbf{B}_0 + \frac{m_e}{e}\frac{\partial \mathbf{j}_e}{\partial t}\right)\right). \tag{B5}$$

Solving for $\mathbf{j}_i$ in Eq. (B3) and inserting the result into Eq. (B4) gives

$$m_i \frac{\partial}{\partial t}\left(\mathbf{j}_e + \frac{\nabla \times \mathbf{B}}{\mu_0 e} - \frac{1}{e}\mathbf{v}_{\rm sat}\,\rho_{\rm sat}(\boldsymbol{\xi})\right) = -e\left(\mathbf{j}_e \times \mathbf{B}_0 + \frac{m_e}{e}\frac{\partial \mathbf{j}_e}{\partial t}\right). \tag{B6}$$

Replacing the time derivative of **B** in Eq. (B6) with the help of Eq. (B5) gives

$$\begin{aligned} m_i \frac{\partial}{\partial t}\left(\mathbf{j}_e - \frac{1}{e}\mathbf{v}_{\rm sat}\,\rho_{\rm sat}(\boldsymbol{\xi})\right) + \frac{m_i}{\mu_0 e}\nabla \\ \times \left(\nabla \times \left(\frac{1}{\tilde{n}(\mathbf{r}_\perp)}\left(\mathbf{j}_e \times \mathbf{B}_0 + \frac{m_e}{e}\frac{\partial \mathbf{j}_e}{\partial t}\right)\right)\right) \\ = -e\left(\mathbf{j}_e \times \mathbf{B}_0 + \frac{m_e}{e}\frac{\partial \mathbf{j}_e}{\partial t}\right), \end{aligned} \tag{B7}$$

which can be rearranged as

$$\begin{aligned} (m_i + m_e)\frac{\partial \mathbf{j}_e}{\partial t} - \frac{m_i}{e}\mathbf{v}_{\rm sat}\frac{\partial}{\partial t}\rho_{\rm sat}(\boldsymbol{\xi}) + \frac{m_i}{\mu_0 e}\nabla \\ \times \left(\nabla \times \left(\frac{\mathbf{j}_e \times \mathbf{B}_0}{\tilde{n}(\mathbf{r}_\perp)} + \frac{m_e}{e\tilde{n}(\mathbf{r}_\perp)}\frac{\partial \mathbf{j}_e}{\partial t}\right)\right) = -e\mathbf{j}_e \times \mathbf{B}_0. \end{aligned} \tag{B8}$$

To solve for $\partial \mathbf{j}_e/\partial t$ the divergence is taken of both sides of Eq. (B8), giving

$$(m_i + m_e)\nabla \cdot \frac{\partial \mathbf{j}_e}{\partial t} - \frac{m_i}{e}\mathbf{v}_{\rm sat} \cdot \nabla \frac{\partial}{\partial t}\rho_{\rm sat}(\boldsymbol{\xi}) = -e\nabla \cdot (\mathbf{j}_e \times \mathbf{B}_0). \tag{B9}$$

Using that $m_i \gg m_e$ and the identity

$$\mathbf{v}_{\rm sat} \cdot \nabla \rho_{\rm sat}(\boldsymbol{\xi}) = -\frac{\partial}{\partial t}\rho_{\rm sat}(\boldsymbol{\xi}) \tag{B10}$$

in Eq. (B9) gives

$$\nabla\cdot\frac{\partial \mathbf{j}_e}{\partial t}=-\frac{1}{e}\frac{\partial^2}{\partial t^2}\rho_{\rm sat}(\boldsymbol{\xi})-\frac{e}{m_i}\nabla\cdot(\mathbf{j}_{\rm e}\times\mathbf{B}_0). \tag{B11}$$

Using the approximation $(1/\tilde{n})(\mathbf{r}_\perp))(\partial \mathbf{j}_e/\partial t)\approx(1/n_0)(\partial \mathbf{j}_e/\partial t)$ and that that $m_i\gg m_e$ in Eq. (B8) gives

$$\frac{\partial \mathbf{j}_e}{\partial t}-\frac{1}{e}\mathbf{v}_{\rm sat}\frac{\partial}{\partial t}\rho_{\rm sat}(\boldsymbol{\xi})+\frac{1}{\mu_0 e}\nabla\times\left(\nabla\times\left(\frac{\mathbf{j}_{\rm e}\times\mathbf{B}_0}{\tilde{n}(\mathbf{r}_\perp)}+\frac{m_e}{en_0}\frac{\partial \mathbf{j}_e}{\partial t}\right)\right)=-\frac{e}{m_i}\mathbf{j}_{\rm e}\times\mathbf{B}_0. \tag{B12}$$

The expansion of double-curl and Eq. (B11) are used to express

$$\nabla\times\left(\nabla\times\frac{\partial \mathbf{j}_e}{\partial t}\right)=\nabla\left(\nabla\cdot\frac{\partial \mathbf{j}_e}{\partial t}\right)-\nabla^2\frac{\partial \mathbf{j}_e}{\partial t}=-\nabla\left(\frac{1}{e}\frac{\partial^2}{\partial t^2}\rho_{\rm sat}(\boldsymbol{\xi})+\frac{e}{m_i}\nabla\cdot(\mathbf{j}_{\rm e}\times\mathbf{B}_0)\right)-\nabla^2\frac{\partial \mathbf{j}_e}{\partial t}, \tag{B13}$$

which inserted into (B12) gives

$$\frac{\partial \mathbf{j}_e}{\partial t}-\frac{1}{e}\mathbf{v}_{\rm sat}\frac{\partial}{\partial t}\rho_{\rm sat}(\boldsymbol{\xi})+\frac{1}{\mu_0 e}\nabla\times\left(\nabla\times\left(\frac{\mathbf{j}_{\rm e}\times\mathbf{B}_0}{\tilde{n}(\mathbf{r}_\perp)}\right)\right)+\frac{m_e}{\mu_0 e^2 n_0}\left[-\nabla\left(\frac{1}{e}\frac{\partial^2}{\partial t^2}\rho_{\rm sat}(\boldsymbol{\xi})+\frac{e}{m_i}\nabla\cdot(\mathbf{j}_{\rm e}\times\mathbf{B}_0)\right)-\nabla^2\frac{\partial \mathbf{j}_e}{\partial t}\right]=-\frac{e}{m_i}\mathbf{j}_{\rm e}\times\mathbf{B}_0. \tag{B14}$$

Using that the factor $m_e/(\mu_0 e^2 n_0)=\lambda_e^2$ and rearranging the terms in Eq. (B14) finally gives

$$\left(1-\lambda_e^2\nabla^2\right)\frac{\partial \mathbf{j}_e}{\partial t}+\frac{\rm e}{m_e}\lambda_{\rm e}^2\nabla\times\left(\nabla\times\left(\frac{\mathbf{j}_{\rm e}\times\mathbf{B}_0}{\tilde{n}(\mathbf{r}_\perp)/n_0}\right)\right)-\frac{e}{m_i}\lambda_{\rm e}^2\nabla(\nabla\cdot(\mathbf{j}_{\rm e}\times\mathbf{B}_0))+\frac{e}{m_i}\mathbf{j}_{\rm e}\times\mathbf{B}_0-\frac{1}{e}\left(\mathbf{v}_{\rm sat}\frac{\partial\rho_{\rm sat}(\boldsymbol{\xi})}{\partial t}+\lambda_e^2\nabla\frac{\partial^2\rho_{\rm sat}(\boldsymbol{\xi})}{\partial t^2}\right)=0, \tag{B15}$$

which is the same as Eq. (5).

APPENDIX C: WEDGE OF LOWER HYBRID WAVES BEHIND A SATELLITE

The formula for maximum parallel group velocities of lower hybrid waves behind a satellite given in Eq. (11) and seen the simulation in Fig. 4 can be derived by considering the group velocity of the satellite-generated lower hybrid waves. In the electrostatic limit ($k\lambda_e\gg 1$) and for quasi-perpendicular lower hybrid waves ($k_\perp\gg k_\parallel$), the dispersion relation (9) reads

$$\omega^2=\omega_{ce}\omega_{ci}+\omega_{ce}^2\frac{k_\parallel^2}{k_\perp^2}. \tag{C1}$$

In the frame of a satellite propagating at an angle to the magnetic field, the Doppler shifted frequency is $\omega'=\omega-k_\perp v_{{\rm sat},\perp}-k_\parallel v_{sat,\parallel}\approx\omega-k_\perp v_{{\rm sat},\perp}$ for $k_\perp\gg k_\parallel$, giving the dispersion relation

$$\left(\omega'+k_\perp v_{{\rm sat},\perp}\right)^2=\omega_{ce}\omega_{ci}+\omega_{ce}^2\frac{k_\parallel^2}{k_\perp^2}. \tag{C2}$$

Groups of lower hybrid waves generated by the satellite are propagating away from the satellite with the group velocity. Taking the derivatives $\partial/\partial k_\parallel$ and $\partial/\partial k_\perp$ of both sides of Eq. (C2) and using that the group velocity components are $v'_{g,\parallel}=\partial\omega'/\partial k_\parallel$ and $v'_{g,\perp}=\partial\omega'/\partial k_\perp$ gives, respectively,

$$2\left(\omega'+k_\perp v_{sat,\perp}\right)v'_{g,\parallel}=2\omega_{ce}^2\frac{k_\parallel}{k_\perp^2}, \tag{C3}$$

$$2\left(\omega'+k_\perp v_{sat,\perp}\right)\left(v'_{g,\perp}+v_{sat,\perp}\right)=-2\omega_{ce}^2\frac{k_\parallel^2}{k_\perp^3}. \tag{C4}$$

In the frame of the satellite, the generated lower hybrid waves are "stationary waves" with zero frequency, $\omega'=0$, so that Eqs. (C1)–(C4) yield

$$k_\perp^2 v_{{\rm sat},\perp}^2=\omega_{ce}\omega_{ci}+\omega_{ce}^2\frac{k_\parallel^2}{k_\perp^2}, \tag{C5}$$

$$v'_{\rm g,\parallel}=\frac{\omega_{ce}^2}{v_{{\rm sat},\perp}}\frac{k_\parallel}{k_\perp^3}, \tag{C6}$$

$$v'_{\rm g,\perp}=-v_{{\rm sat},\perp}-\frac{\omega_{\rm ce}^2}{v_{{\rm sat},\perp}}\frac{k_\parallel^2}{k_\perp^4}, \tag{C7}$$

respectively. Using Eqs. (C6) and (C7), the angle φ of the group velocity to the magnetic field for the waves behind the satellite is obtained from

$$\tan\varphi=\left|\frac{v'_{\rm g,\perp}}{v'_{\rm g,\parallel}}\right|=\left(\frac{k_\perp^2 v_{{\rm sat},\perp}^2}{\omega_{\rm ce}^2}+\frac{k_\parallel^2}{k_\perp^2}\right)\frac{k_\perp}{k_\parallel}. \tag{C8}$$

Using Eq. (C5) to eliminate $k_\perp^2 v_{{\rm sat},\perp}^2$ in Eq. (C8) gives

$$\tan\varphi=\left(2\frac{k_\parallel^2}{k_\perp^2}+\frac{\omega_{ci}}{\omega_{ce}}\right)\frac{k_\perp}{k_\parallel}=2\frac{k_\parallel}{k_\perp}+\frac{\omega_{ci}}{\omega_{ce}}\frac{k_\perp}{k_\parallel}. \tag{C9}$$

It is readily found that $\tan\varphi$ in Eq. (C9) as a function of $k_\parallel/k_\perp$ has a minimum for

$$\frac{k_\parallel}{k_\perp}=\sqrt{\frac{\omega_{ci}}{2\omega_{ce}}}. \tag{C10}$$

Inserting this expression in Eq. (C9) gives

$$\tan\varphi=\left|\frac{v'_{\rm g,\perp}}{v'_{\rm g,\parallel}}\right|=\sqrt{\frac{8\omega_{ci}}{\omega_{ce}}}. \tag{C11}$$

This forms a cone behind the satellite, and in the frame of the plasma, one has the lower hybrid waves confined within the wedge

$$|v_\parallel|<v_{{\rm sat},\perp}\sqrt{\frac{\omega_{\rm ce}}{8\omega_{\rm ci}}}, \tag{C12}$$

which is given in Eq. (11) and indicated in Fig. 4.

APPENDIX D: TEMPERATURE EFFECTS ON LOWER HYBRID WAVES

In the electrostatic approximation ($\mathbf{E} = -\nabla\phi$) the dispersion relation can be written $\epsilon = 0$, where $\epsilon = 1 + \chi_i + \chi_e$ is the dielectric constant and χ_i and χ_e are the electron and ion susceptibilities. Assuming quasi-neutrality $n_i = n_e$, which is justified when $\omega_{pe}^2 \gg \omega_{ce}^2$, simplifies the dispersion relation as

$$\chi_i + \chi_e = 0. \tag{D1}$$

In a warm fluid model for magnetized plasma, the ion and electron susceptibilities are

$$\chi_i = -\frac{\omega_{pi}^2\left(k^2\omega^2 - k_\parallel^2\omega_i^2\right)}{k^2\left[\omega^2\left(\omega^2 - \omega_{ci}^2\right) - \gamma_i v_{Ti}^2\left(k^2\omega^2 - k_\parallel^2\omega_{ci}^2\right)\right]}, \tag{D2}$$

$$\chi_e = -\frac{\omega_{pe}^2\left(k^2\omega^2 - k_\parallel^2\omega_{ce}^2\right)}{k^2\left[\omega^2\left(\omega^2 - \omega_{ce}^2\right) - \gamma_e v_{Te}^2\left(k^2\omega^2 - k_\parallel^2\omega_{ce}^2\right)\right]}, \tag{D3}$$

where $v_{Ti} = \sqrt{k_B T_i/m_i}$ and $v_{Te} = \sqrt{k_B T_e/m_e}$ are the ion and electron thermal speeds, T_i and T_e the electron and ion temperatures, and γ_i and γ_e are the adiabatic indices for ions and electrons, respectively. We assume $\gamma_i = 3$ for one-dimensional ion fluid compression and $\gamma_e = 1$ for isothermal electrons.

For lower hybrid waves, one has $\omega_{ci}^2 \ll \omega^2$, so that the ion susceptibility (using $\gamma_i = 3$) simplifies to

$$\chi_i \approx -\frac{\omega_{pi}^2}{\omega^2 - 3v_{Ti}^2k^2}. \tag{D4}$$

For the electrons, one may assume $\omega^2 \ll \omega_{ce}^2$ for quasi-perpendicular waves (and $\gamma_e = 1$), giving

$$\chi_e \approx \frac{\omega_{pe}^2\left(k^2\omega^2 - k_\parallel^2\omega_{ce}^2\right)}{k^2\left[\omega^2\omega_{ce}^2 + v_{Te}^2\left(k^2\omega^2 - k_\parallel^2\omega_{ce}^2\right)\right]}. \tag{D5}$$

Inserting the approximate χ_i and χ_e into Eq. (D1) gives the dispersion relation

$$-\frac{\omega_{pi}^2}{\omega^2 - 3v_{Ti}^2k^2} + \frac{\omega_{pe}^2\left(k^2\omega^2 - k_\parallel^2\omega_{ce}^2\right)}{k^2\left[\omega^2\omega_{ce}^2 + v_{Te}^2\left(k^2\omega^2 - k_\parallel^2\omega_{ce}^2\right)\right]} = 0, \tag{D6}$$

which can be reorganized as

$$\omega^4 - \omega^2\left(\omega_{LH}^2 + \frac{k_\parallel^2}{k^2}\omega_{ce}^2 + C_s^2k^2\right) + \omega_{ce}^2C_s^2k_\parallel^2 = 0, \tag{D7}$$

where $C_s = \sqrt{k_B(T_e + 3T_i)/m_i}$ is the ion sound speed and $\omega_{LH} = \sqrt{\omega_{ci}\omega_{ce}}$ is the lower hybrid frequency. One has $C_s \approx 1.5\,\mathrm{km/s}$ for typical temperatures $T_e = 1500\,\mathrm{K}$ and $T_i = 1000\,\mathrm{K}$. Assuming $C_s^2k^2$ to be small compared to other terms, the solution, to lowest order in $C_s^2k^2$, is

$$\omega^2 \approx \omega_{LH}^2 + \frac{k_\parallel^2}{k^2}\omega_{ce}^2 + \frac{C_s^2k^2\omega_{LH}^2}{\omega_{LH}^2 + k_\parallel^2\omega_{ce}^2/k^2}, \tag{D8}$$

consistent with Eq. (9) in the cold plasma limit $C_s = 0$. It is seen in Eq. (D8) that the thermal corrections are important only for large wavenumbers such that C_s becomes comparable to the phase speed ω/k of the wave, as indicated in Fig. 2.

APPENDIX E: DETAILS IN THE NUMERICAL SIMULATION METHOD OF WAVE EQ. (5)

The solutions of the wave equation (5) are represented on a 2D rectangular domain in the y–z plane spanned by $-2\,\mathrm{km} < y < 2\,\mathrm{km}$ and $-10\,\mathrm{km} < z < 10\,\mathrm{km}$, and are resolved on a numerical grid with periodic boundary conditions in both directions. For numerical efficiency, the grid size in the z-direction is $\Delta z = 50\,\mathrm{m}$ to resolve the artificially elongated satellite model described in Sec. V A, while the grid size in the y-direction is adapted to resolve the lower hybrid wavelength ($\lambda_{\mathrm{LH}} \sim 1\,\mathrm{m}$) and the smallest of the striation and satellite widths, $D_{\min} = \min(D_{\mathrm{str}}, D_{\mathrm{sat}})$; the grid size $\Delta y = 0.2\,\mathrm{m}$ is used for $D_{\min} \geq 0.5\,\mathrm{m}$, $\Delta y = 0.1\,\mathrm{m}$ for $D_{\min} = 0.25\,\mathrm{m}$, $\Delta y = 0.02\,\mathrm{m}$ for $D_{\min} = 0.1\,\mathrm{m}$, and $\Delta y = 0.01\,\mathrm{m}$ for $D_{\min} = 0.05\,\mathrm{m}$. All space derivatives in Eq. (5) are approximated with second-order centered difference approximations using periodic boundary conditions. The difference approximations have been implemented to run on high-performance computing (HPC) clusters using domain decomposition and message passing interface (MPI); typically 40–80 processors are used. The inversion of the $\left(1 - \lambda_e^2\nabla^2\right)$ operator in Eq. (5) is done using the conjugate gradient (CG) method [e.g., Strikwerda (1989)] with a preconditioner based on applying the inverse of a numerical approximation (using centered difference approximations) of the factorized operator $\left(1 - \lambda_e^2\partial^2/\partial z^2\right)\left(1 - \lambda_e^2\partial^2/\partial y^2\right)$ on all terms. The resulting tridiagonal systems are solved using a parallel solver [e.g., Bondeli (1991); Eliasson (2005); and Kim *et al.* (2021)]. Typically $3 - 4$ CG iterations are necessary for convergence. The solution is advanced in time using the standard 4th-order Runge–Kutta method using the time step $\Delta t = \mathrm{CFL}\sqrt{8}/\omega_{\max}$ (Courant–Friedrichs–Lewy)where the maximum frequency $\omega_{\max}$ is obtained by finding the maximum ω in Eq. (6) for wave vectors $k_\parallel < 2/\Delta z$ and $k_\perp < 2/\Delta y$, and $\mathrm{CFL} = 0.9 < 1$ for numerical stability. The region $|z| > 5\,\mathrm{km}$ is used to damp out fast whistler waves and prevent them from exiting and reentering the domain multiple times through the periodic boundary conditions.

REFERENCES

Anderson, P. C., "Characteristics of spacecraft charging in low Earth orbit," J. Geophys. Res. **117**, A07308, https://doi.org/10.1029/2011JA016875 (2012).

Arshad, K., Mahmood, S., and Mirza, A. M., "Landau damping of ion acoustic wave in Lorentzian multi-ion plasmas," Phys. Plasmas **18**(9), 092115 (2011).

Bamber, J. F., Gekelman, W., and Maggs, J. E., "Whistler wave mode conversion to lower hybrid waves at a density striation," Phys. Rev. Lett. **73**, 2990 (1994).

Bamber, J. F., Maggs, J. E., and Gekelman, W., "Whistler wave interaction with a density striation: A laboratory investigation of an auroral process," J. Geophys. Res. **100**(A12), 23795–23810, https://doi.org/10.1029/95JA01852 (1995).

Beckers, J., Berndt, J., Block, D., Bonitz, M., Bruggeman, P. J., Couëdel, L., Delzanno, G. L., Feng, Y., Gopalakrishnan, R., Greiner, F., Hartmann, P., Horányi, M., Kersten, H., Knapek, C. A., Konopka, U., Kortshagen, U., Kostadinova, E. G., Kovačević, E., Krasheninnikov, S. I., Mann, I., Mariotti, D., Matthews, L. S., Melzer, A., Mikikian, M., Nosenko, V., Pustylnik, M. Y., Ratynskaia, S., Sankaran, R. M., Schneider, V., Thimsen, E. J., Thomas, E.,

Thomas, H. M., Tolias, P., and van de Kerkhof, M., "Physics and applications of dusty plasmas: The perspectives 2023," Phys. Plasmas **30**, 120601 (2023).
Bell, T. F. and Ngo, H. D., "Electrostatic lower hybrid waves excited by electromagnetic whistler mode waves scattering from planar magnetic field-aligned plasma density irregularities," J. Geophys. Res. **95**, 149–172, https://doi.org/10.1029/JA095iA01p00149 (1990).
Bernhardt, P. A., Ganguli, G., Kelley, M. C., and Swartz, W. E., "Enhanced radar backscatter from space shuttle exhaust in the ionosphere," J. Geophys. Res. **100**(A12), 23811–23818, https://doi.org/10.1029/95JA02836 (1995a).
Bernhardt, P. A., Hua, M., Bortnik, J., Ma, Q., Verronen, P. T., McCarthy, M. P., Hampton, D. L., Golkowski, M., Cohen, M. B., Richardson, D. K., Howarth, A. D., James, H. G., and Meredith, N. P., "Active precipitation of radiation belt electrons using rocket exhaust driven amplification (REDA) of man-made whistlers," J. Geophys. Res.: Space Phys. **127**(6), e2022JA030358, https://doi.org/10.1029/2022JA030358 (2022).
Bernhardt, P. A., Scott, L., Howarth, A., and Morales, G. J., "Observations of plasma waves generated by charged space objects," Phys. Plasmas **30**, 092106 (2023).
Bernhardt, P. A., Siefring, C. L., Rodriguez, P., Haas, D. G., Baumback, M. M., Romero, H. A., Solin, D. A., Djuth, F. T., Duncan, L. M., Hunton, D. E., Pollock, C. J., Sulzer, M. P., Tepley, C. A., Wagner, L. S., and Goldstein, J. A., "The ionospheric focused heating experiment," J. Geophys. Res. **100**(A9), 17331–17345, https://doi.org/10.1029/94JA01887 (1995b).
Blackwell, D. D., Walker, D. N., Messer, S. J., and Amatucci, W. E., "Characteristics of the plasma impedance probe with constant bias," Phys. Plasmas **12**, 093510 (2005).
Bondeli, S., "Divide and conquer: A parallel algorithm for the solution of a tridiagonal linear system of equations," Parallel Comput. **17**(4–5), 419–434 (1991).
Bujarbarua, S. and Schamel, H., "Theory of finite-amplitude electron and ion holes," J. Plasma Phys. **25**(3), 515–529 (1981).
Camporeale, E., Delzanno, G. L., and Colestock, P., "Lower hybrid to whistler mode conversion on a density striation," J. Geophys. Res. **117**, A10315, https://doi.org/10.1029/2012JA017726 (2012).
Chen, F. F., "Electric probes," in *Plasma Diagnostic Techniques*, edited by Huddlestone, R. H. and Leonard, S. L. (Academic, New York, 1965).
Chen, F. F., *Introduction to Plasma Physics and Controlled Fusion*, 2nd ed. (Plenum, New York, 1984), Chap. 7.
Eliasson, B., "The parallel implementation of the one-dimensional Fourier transformed Vlasov–Poisson system," Comput. Phys. Commun. **170**, 205–230 (2005).
Eliasson, B. and Papadopoulos, K., "Numerical study of mode conversion between lower hybrid and whistler waves on short-scale density striations," J. Geophys. Res. **113**, A09315, https://doi.org/10.1029/2008JA013261 (2008).
Fiser, J., Chum, J., Diendorfer, G., Parrot, M., and Santolik, O., "Whistler intensities above thunderstorms," Ann. Geophys. **28**, 37–46 (2010).
Fried, B. D. and Conte, S. D., *The Plasma Dispersion Function* (Academic Press, New York, 1961).
Garrett, H. B., "The charging of spacecraft surfaces," Rev. Geophys. **19**(4), 577–616, https://doi.org/10.1029/RG019i004p00577 (1981).
Grach, S., Sergeev, E. N., Mishin, E. V., and Shindin, A. V., "Dynamic properties of ionospheric plasma turbulence driven by high-power high-frequency radiowaves," Phys.-Usp. **59**(11), 1091–1128 (2016).
Hall, J. O., "Conversion of localized lower hybrid oscillations and fast magnetosonic waves at a plasma density cavity," Phys. Plasmas **11**, 5341–5349 (2004).
Hall, J. O., Eriksson, A. I., and Leyser, T. B., "Excitation of localized rotating waves in plasma density cavities by scattering of fast magnetosonic waves," Phys. Rev. Lett. **92**(25), 255002 (2004).
Helliwell, R. A., *Whistlers and Related Ionospheric Phenomena* (Stanford University Press, 1965).
Huba, J. D., *NRL Plasma Formulary* (NRL, Washington, DC, 1994).
Hutchinson, I. H., *Principles of Plasma Diagnostics*, 2nd ed. (Cambridge University Press, Cambridge, 2002), Chap. 3.
Ikezi, H., Taylor, R. J., and Baker, D. R., "Formation and interaction of ion-acoustic solitions," Phys. Rev. Lett. **25**, 11–14 (1970).
James, H. G., King, E. P., White, A., Hum, R. H., Lunscher, W. H. H. L., and Siefring, C. L., "The e-POP radio receiver instrument on CASSIOPE," Space Sci. Rev. **189**, 79–105 (2015).
Kelley, M. C., Arce, T. L., Salowey, J., Sulzer, M., Armstrong, W. T., Carter, M., and Duncan, L., "Density depletions at the 10-m scale induced by the Arecibo heater," J. Geophys. Res. **100**(A9), 17367–17376, https://doi.org/10.1029/95JA00063 (1995).
Kim, K.-H., Kang, J.-H., Pan, X., and Choi, J.-I., "PaScaL_TDMA: A library of parallel and scalable solvers for massive tridiagonal systems," Comput. Phys. Commun. **260**, 107722 (2021).
Kumar, A. and Sen, A., "Precursor magneto-sonic solitons in a plasma from a moving charge bunch," New J. Phys. **22**, 073057 (2020).
Laframboise, J. G., "Theory of spherical and cylindrical langmuir probes in a collisionless, Maxwellian plasma at rest," Ph.D. thesis (University of Toronto, Institute for Aerospace Studies, 1966), UTIAS Report No. 100.
Langmuir, I. and Mott-Smith, H., "The theory of collectors in gaseous discharges," Phys. Rev. **28**, 727–763 (1926).
Lorimer, D. R. and Kramer, M., *Handbook of Pulsar Astronomy* (Cambridge University Press, Cambridge, UK, 2005).
Manchester, Z., "Measurement and analysis of the capacitance of charged objects in a plasma with applications to Lorentz-actuated spacecraft," M.Eng. Report (Cornell University, Ithaca, NY, 2010), see http://zacmanchester.github.io/docs/Zac_Manchester_MEng_Report.pdf
McKinstrie, C. J., Giacone, R. E., and Startsev, E. A., "Accurate formulas for the landau damping rates of electrostatic waves," Phys. Plasmas **6**(2), 463–466 (1999).
Merlino, R. L., "Understanding Langmuir probe current-voltage characteristics," Am. J. Phys. **75**, 1078–1085 (2007).
Najmi, A., Milikh, G., Secan, J., Chiang, K., Psiaki, M., Bernhardt, P., Briczinski, S., Siefring, C., Chang, C. L., and Papadopoulos, K., "Generation and detection of super small striations by F region HF heating," J. Geophys. Res.: Space Phys. **119**, 6000–6010, https://doi.org/10.1002/2014JA020038 (2014).
Najmi, A., Milikh, G., Yampolski, Y. M., Koloskov, A. V., Sopin, A. A., Zalizovski, A., Bernhardt, P., Briczinski, S., Siefring, C., Chiang, K., Morton, Y., Taylor, S., Mahmoudian, A., Bristow, W., Ruohoniemi, M., and Papadopoulos, K., "Studies of the ionospheric turbulence excited by the fourth gyroharmonic at HAARP," J. Geophys. Res.: Space Phys. **120**, 6646–6660, https://doi.org/10.1002/2015JA021341 (2015).
Ott, E. and Sudan, R. N., "Nonlinear theory of ion acoustic waves with Landau damping," Phys. Fluids **12**, 2388–2394 (1969).
Pécseli, H. L., Armstrong, R. J., and Trulsen, J., "Experimental observations of ion phase-space vortices," Phys. Lett. A **81**(7), 386–390 (1981).
Pécseli, H. L., Trulsen, J., and Armstrong, R. J., "Formation of ion phase-space vortexes," Phys. Scr. **29**(3), 241–253 (1984).
Rao, N. N., Shukla, P. K., and Yu, M. Y., "Dust-acoustic waves in dusty plasmas," Planet. Space Sci. **38**, 543–546 (1990).
Rosenberg, S. and Gekelman, W., "Electric field measurements of directly converted lower hybrid waves at a density striation," Geophys. Res. Lett. **25**(6), 865–868, https://doi.org/10.1029/98GL00382 (1998).
Rosenberg, S. and Gekelman, W., "A laboratory investigation of lower hybrid wave interactions with a field-aligned density depletion," Geophys. Res. Lett. **27**(6), 859–862, https://doi.org/10.1029/1999GL000005 (2000).
Rosenberg, S. and Gekelman, W., "A three-dimensional experimental study of lower hybrid wave interactions with field aligned density depletions," J. Geophys. Res. **106**(A12), 28867–28884, https://doi.org/10.1029/2000JA000061 (2001).
Saitou, Y. and Nakamura, Y., "Ion-acoustic soliton-like waves undergoing Landau damping," Phys. Lett. A **343**, 397–402 (2005).
Schamel, H. and Bujarbarua, S., "Solitary plasma hole via ion-vortex distribution," Phys. Fluids **23**, 2498–2499 (1980).
Sen, A., Tiwari, S., Mishra, S., and Kaw, P., "Nonlinear wave excitations by orbiting charged space debris objects," Adv. Space Res. **56**(3), 429–435 (2015).
Shao, X., Eliasson, B., Sharma, A. S., Milikh, G., and Papadopoulos, K., "Attenuation of whistler waves through conversion to lower hybrid waves in the low-altitude ionosphere," J. Geophys. Res. **117**, A04311, https://doi.org/10.1029/2011JA017339 (2012).
Shukla, P. K. and Eliasson, B., "*Colloquium*: Fundamentals of dust-plasma interactions," Rev. Mod. Phys. **81**, 25–44 (2009).
Stix, T. H., *Waves in Plasmas* (AIP, Melville, NY, 1992).
Strikwerda, J. C., *Finite Difference Schemes and Partial Differential Equations* (Chapman & Hall, New York, 1989), Chap. 14.

Swanson, D. G., *Plasma Waves*, 2nd ed. (IOP, Bristol and Philadelphia, 2003).
Taniuti, T., "Nonlinear ion-acoustic waves with ion Landau damping," J. Phys. Soc. Jpn. **33**(1), 277 (1972).
Tiwari, S. K. and Sen, A., "Wakes and precursor soliton excitations by a moving charged object in a plasma," Phys. Plasmas **23**(2), 022301 (2016).
Tran, M. Q., "Ion acoustic solitons in a plasma: A review of their experimental properties and related theories," Phys. Scr. **20**, 317–327 (1979).
Truitt, A. S. and Hartzell, C. M., "Simulating plasma solitons from orbital debris using the forced Korteweg–de Vries equation," J. Spacecr. Rockets **57**(5), 876–897 (2020a).
Truitt, A. S. and Hartzell, C. M., "Simulating damped ion acoustic solitary waves from orbital debris," J. Spacecr. Rockets **57**(5), 975–984 (2020b).
VanDam, J. W. and Taniuti, T., "Nonlinear ion acoustic waves with Landau damping," J. Phys. Soc. Jpn. **35**(3), 897–906 (1973).
Wang, R., Vasko, I. Y., Mozer, F. S., Bale, S. D., Artemyev, A. V., Bonnell, J. W., Ergun, R., Giles, B., Lindqvist, P.-A., Russell, C. T., and Strangeway, R., "Electrostatic turbulence and Debye-scale structures in collisionless shocks," Astrophys. J. Lett. **889**, L9 (2020).
Whipple, E. C., "Potentials of surfaces in space," Rep. Prog. Phys. **44**, 1197 (1981).